

1 LEVERAGING MULTI-MESSENGER ASTROPHYSICS FOR DARK MATTER SEARCHES

By

Daniel Nicholas Salazar-Gallegos

A DISSERTATION

Submitted to
Michigan State University
in partial fulfillment of the requirements
for the degree of

Physics—Doctor of Philosophy
Computational Mathematics in Science and Engineering—Dual Major

Today

ABSTRACT

3 I did Dark Matter with HAWC and IceCube. I also used Graph Neural Networks

⁴ Copyright by

⁵ DANIEL NICHOLAS SALAZAR-GALLEGOS

⁶ Today

ACKNOWLEDGMENTS

8 I love my friends. Thanks to everyone that helped me figure this out. Amazing thanks to the people
9 at LANL who supported me. Eames, etc Dinner Parties Jenny and her child Kaydince Kirsten, Pat,
10 Andrea Family. You're so far but so critical to my formation. Unconditional love. Roommate

TABLE OF CONTENTS

| | | |
|----|--|------|
| 12 | LIST OF TABLES | vii |
| 13 | LIST OF FIGURES | viii |
| 14 | LIST OF ABBREVIATIONS | xi |
| 15 | CHAPTER 1 INTRODUCTION | 1 |
| 16 | CHAPTER 2 DARK MATTER IN THE COSMOS | 2 |
| 17 | 2.1 Introduction | 2 |
| 18 | 2.2 Dark Matter Basics | 3 |
| 19 | 2.3 Evidence for Dark Matter | 4 |
| 20 | 2.4 Searching for Dark Matter: Particle DM | 11 |
| 21 | 2.5 Sources for Indirect Dark Matter Searches | 16 |
| 22 | 2.6 Multi-Messenger Dark Matter | 18 |
| 23 | CHAPTER 3 MULTIMESSENGER ASTROPHYSICS: DETECTING HIGH EN- | |
| 24 | ERGY NEUTRAL MESSENGERS | 21 |
| 25 | 3.1 Introduction | 21 |
| 26 | 3.2 Charged Particles in a Medium | 21 |
| 27 | 3.3 Photons (γ) | 22 |
| 28 | 3.4 Neutrinos (ν) | 22 |
| 29 | 3.5 Opportunities to Combine for Dark Matter | 22 |
| 30 | CHAPTER 4 HIGH ALTITUDE WATER CHERENKOV (HAWC) OBSERVATORY . | 24 |
| 31 | 4.1 The Detector | 24 |
| 32 | 4.2 Events Reconstruction and Data Acquisition | 24 |
| 33 | 4.3 Remote Monitoring | 24 |
| 34 | CHAPTER 5 ICECUBE NEUTRINO OBSERVATORY | 25 |
| 35 | 5.1 The Detector | 25 |
| 36 | 5.2 Events Reconstruction and Data Acquisition | 25 |
| 37 | 5.3 Northern Test Site | 25 |
| 38 | CHAPTER 6 COMPUTATIONAL TECHNIQUES IN PARTICLE ASTROPHYSICS . | 26 |
| 39 | 6.1 Neural Networks for Gamma/Hadron Separation | 26 |
| 40 | 6.2 Parallel Computing for Dark Matter Analyses | 26 |
| 41 | CHAPTER 7 GLORY DUCK | 27 |
| 42 | 7.1 Dataset and Background | 27 |
| 43 | 7.2 Analysis | 29 |
| 44 | 7.3 HAWC Results | 34 |
| 45 | CHAPTER 8 NU DUCK | 38 |

| | | |
|----|------------------------|----|
| 46 | BIBLIOGRAPHY | 39 |
|----|------------------------|----|

LIST OF TABLES

| | |
|---|-----------------|
| 48 Table 7.1 Summary of the relevant properties of the dSphs used in the present work. 49 Column 1 lists the dSphs. Columns 2 and 3 present their heliocentric distance 50 and galactic coordinates, respectively. Columns 4 and 5 report the J -factors of 51 each source given from the \mathcal{GS} and \mathcal{B} independent studies and their estimated 52 $\pm 1\sigma$ uncertainties. The values $\log_{10} J$ (\mathcal{GS} set) [30] correspond to the mean 53 J -factor values for a source extension truncated at the outermost observed star. 54 The values $\log_{10} J$ (\mathcal{B} set) [31] are provided for a source extension at the tidal 55 radius of each dSph. Bolded sources are within HAWC's field of view and 56 provided to the Glory Duck analysis. | 31 |
| 57 Table 7.2 Summary of dSph observations by each experiment used in this work. A 58 ‘-’ indicates the experiment did not observe the dSph for this study. For 59 Fermi-LAT, the exposure at 1 GeV is given. For HAWC, $ \Delta\theta $ is the absolute 60 difference between the source declination and HAWC latitude. HAWC is more 61 sensitive to sources with smaller $ \Delta\theta $. For IACTs, we show the zenith angle 62 range, the total exposure, the energy range, the angular radius θ of the signal or 63 ON region, the ratio of exposures between the background-control (OFF) and 64 signal (ON) regions (τ), and the significance of gamma-ray excess in standard 65 deviations, σ . | 32 |
| 66 Proof I know how to include | |

LIST OF FIGURES

| | | | |
|----|------------|---|----|
| 68 | Figure 2.1 | Rotation curve fit to NGC 6503 from [7]. Dashed line is the contribution 69 from visible matter. Dotted curves are from gas. Dash-dot curves are from 70 dark matter (DM). Solid line is the composite contribution from all matter 71 and DM sources. Data are indicated with bold dots with error bars. Data 72 agree strongly with a matter + DM composite prediction. | 5 |
| 73 | Figure 2.2 | Light from distant galaxy is bent in unique ways depending on the distribution 74 of mass between the galaxy and Earth. Yellow dashed lines indicate where 75 the light would have gone if the matter were not present [8]. | 7 |
| 76 | Figure 2.3 | (left) Optical image of galactic cluster 1E0657-558. (right) X-ray image of the 77 cluster with redder meaning hotter and higher baryon density. (both) Green 78 contours are reconstruction of gravity contours from weak lensing. White 79 rings are the best fit mass maxima at 68.3%, 95.5%, and 99.7% confidence. 80 The matter maxima of the clusters are clearly separated from x-ray maxima. [9] | 8 |
| 81 | Figure 2.4 | Plank CMB sky. Sky map features small variations in temperature in primor- 82 dial light. These anisotropies are used to make inferences about the universe's 83 energy budget and developmental history. [10] | 9 |
| 84 | Figure 2.5 | Observed Cosmic Microwave Background power spectrum as a function of 85 multipole moment from Plank [10]. Blue line is best fit model from Λ CDM. 86 Red points and lines are data and error, respectively. | 10 |
| 87 | Figure 2.6 | Predicted power spectra of CMB for different $\Omega_m h^2$ values for fixed baryon 88 density from [11]. (left) Low $\Omega_m h^2$ increases the prominence of first and 89 second peaks. (middle) $\Omega_m h^2$ is most similar to the observed power spectrum. 90 The second and third peaks are similar in height. (right) $\Omega_m h^2$ is large which 91 suppresses the first peak and raises the prominence of the third peak. | 10 |
| 92 | Figure 2.7 | The Standard Model (SM) of particle physics. Figure taken from http://www.quantumdiaries.org/2014/03/14/the-standard-model-a-beautiful-but-flawed-theory/ | 12 |
| 95 | Figure 2.8 | Simplified Feynman diagram demonstrating with different ways DM can 96 interact with SM particles. The 'X's refer to the DM particles whereas the 97 SM refer to fundamental particles in the SM. The large circle in the center 98 indicates the vertex of interaction and is purposely left vague. The colored 99 arrows refer to different directions of time as well as their respective labels. 100 The arrows indicate the initial and final state of the DM -SM interaction in time. | 13 |

| | | |
|-----|--|----|
| 101 | Figure 2.9 A single jet event in ATLAS detector from 2017 [16]. Jet momentum was 102 observed to be 1.9 TeV. Missing transverse momentum was observed to be 103 1.9 TeV compared to the initial transverse momentum of the event was 0. 104 Implied MET is traced by a red dashed line in event display. | 14 |
| 105 | Figure 2.10 More detailed pseudo-Feynman diagram of particle cascade from dark matter 106 annihilation into 2 quarks. The quarks hadronize and down to stable particles 107 like γ or the anti-proton (p^-). Diagram pulled from ICRC 2021 presentation 108 on DM annihilation search [17]. | 15 |
| 109 | Figure 2.11 Dark Matter (DM) decay spectrum for $b\bar{b}$ initial state and γ final state. Redder 110 spectra are for larger DM masses. Bluer spectra are light DM masses. x is a 111 unitless factor defined as the ratio of the mass of DM, m_χ , and the final state 112 particle energy E_γ . Figure from [19]. | 17 |
| 113 | Figure 2.12 Different dark matter density profiles compared. Some models produce ex- 114 ceptionally large densities at small r [20]. | 18 |
| 115 | Figure 2.13 The Milky Way Galaxy in photons (γ) and neutrinos (ν) [22]. The Galactic 116 center is at $l=0^\circ$ and is the brightest region in all panels. (top) An Optical 117 color image of the Milky Way galaxy seen from Earth. Clouds of gas and dust 118 obscure some light from stars. (2nd down) Integrated flux of γ -rays observed 119 by the Fermi-LAT telescope [23]. (middle) Expected neutrino emission 120 that corresponds with Fermi-LAT observations. (2nd up) Expected neutrino 121 emission profile after considering detector systematics of IceCube. (bottom) 122 Observed neutrino emission from region of the galactic plane. Substantial 123 neutrino emission was detected. | 19 |
| 124 | Figure 2.14 Dark Matter annihilation spectra for different final state particle and standard 125 model annihilation channels [24]. Photons (red), e^\pm (green), \bar{p} (blue), ν (black). | 20 |
| 126 | Figure 3.1 TODO: Show a nuclear reactor with cherenkov radiation[NEEDS A SOURCE][FACT 127 CHECK THIS] | 22 |
| 128 | Figure 3.2 TODO: absorption spectrum of liquid and solid water[NEEDS A SOURCE][FACT 129 CHECK THIS] | 23 |

| | | |
|-----|---|----|
| 130 | Figure 7.1 Illustration of the combination technique showing a comparison between 131 $-2 \ln \lambda$ provided by four instruments (colored lines) from the observation 132 of the same dSph without any J nuisance and their sum, <i>i.e.</i> the resulting 133 combined likelihood (thin black line). According to the test statistics of 134 Equation (7.6), the intersection of the likelihood profiles with the line $-2 \ln \lambda$ 135 = 2.71 indicates the 95% C.L. upper limit on $\langle \sigma v \rangle$. The combined likeli- 136 hood (thin black line) shows a smaller value of upper limit on $\langle \sigma v \rangle$ than 137 those derived by individual instruments. We also show the uncertainties on 138 the J -factor affects the combined likelihood and degrade the upper limit on 139 $\langle \sigma v \rangle$ (thick black line). All likelihood profiles are normalized so that the 140 global minimum $\langle \sigma v \rangle$ is 0. We note that each profile depends on the observa- 141 tional conditions in which a target object was observed. The sensitivity of a 142 given instrument can be degraded and the upper limits less constraining if the 143 observations are performed in non optimal conditions such as a high zenith 144 angle or a short exposure time. | 34 |
| 145 | Figure 7.2 HAWC upper limits at 95% confidence level on $\langle \sigma v \rangle$ versus DM mass for 146 seven annihilation channels, using the set of J -factors from Ref. [29] The 147 solid line represents the observed combined limit. Dashed lines represent 148 limits from individual dSphs. | 36 |
| 149 | Figure 7.3 HAWC Brazil bands at 95% confidence level on $\langle \sigma v \rangle$ versus DM mass for 150 seven annihilation channels with J -factors from GS [29]. The solid line 151 represents the combined limit from 13 dSphs. The dashed line is the expected 152 limit. The green band is the 68% containment. The yellow band is the 95% 153 containment. | 37 |

LIST OF ABBREVIATIONS

- 155 **MSU** Michigan State University
156 **LANL** Los Alamos National Laboratory
157 **DM** Dark Matter
158 **SM** Standard Model
159 **HAWC** High Altitude Water Cherenkov Observatory

160

CHAPTER 1

INTRODUCTION

161 Is the text not rendering right? Ah ok it knows im basically drafting the doc still

CHAPTER 2

162

DARK MATTER IN THE COSMOS

163 **2.1 Introduction**

164 The dark matter problem can be summarized in part by the following thought experiment.

165 Let us say you are the teacher for an elementary school classroom. You take them on a field
166 trip to your local science museum and among the exhibits is one for mass and weight. The exhibit
167 has a gigantic scale, and you come up with a fun problem for your class.

168 You ask your class, "What is the total weight of the classroom? Give your best estimation to
169 me in 30 minutes, and then we'll check your guess on the scale. If your guess is within 10% of the
170 right answer, we will stop for ice cream on the way back."

171 The students are ecstatic to hear this, and they get to work. The solution is some variation of
172 the following strategy. The students should give each other their weight or best guess if they do
173 not know. Then, all they must do is add each student's weight and get a grand total for the class.

174 The measurement on the giant scale should show the true weight of the class. When comparing
175 the measured weight to your estimation, multiply the measurement by 1.0 ± 0.1 to get the $\pm 10\%$
176 tolerances for your estimation.

177 Two of your students, Sandra and Mario, return to you with a solution.

178 They say, "We weren't sure of everyone's weight. We used 65 lbs. for the people we didn't
179 know and added everyone who does know. There are 30 of us, and we got 2,000 lbs.! That's a ton!"

180 You estimated 1,900 lbs. assuming the average weight of a student in your class was 60 lbs.
181 So, you are pleased with Sandra's and Mario's answer. You instruct your students to all gather on
182 the giant scale and read off the weight together. To all your surprise, the scale reads *10,000 lbs.!*
183 10,000 is significantly more than a 10% error from 2,000. In fact, it is approximately 5 times more
184 massive than either your or your students' estimates. You think to yourself and conclude there
185 must be something wrong with the scale. You ask an employee to check the scale and verify it is
186 well calibrated. They confirm that the scale is in working order. You weigh a couple of students
187 individually to assess that the scale is well calibrated. Sandra weighs 59 lbs., and Mario weighs

188 62 lbs., typical weights for their age. You then weigh each student individually and see that their
189 weights individually do not deviate greatly from 60 lbs. So, where does all the extra weight come
190 from?

191 This thought experiment serves as an analogy to the Dark Matter problem. The important
192 substitution to make however is to replace the students with stars and the classroom with a galaxy,
193 say the Milky Way. Individually the mass of stars is well measured and defined with the Sun as our
194 nearest test case. However, when we set out to measure the mass of a collection of stars as large as
195 galaxies, our well-motivated estimation is wildly incorrect. There simply is no way to account for
196 this discrepancy except without some unseen, or dark, contribution to mass and matter in galaxies.
197 I set out in my thesis to narrow the possibilities of what this Dark Matter could be.

198 This chapter is organized like the following... **TODO: Text should look like ... Chapter x has**
199 **blah blah blah.**

200 2.2 Dark Matter Basics

201 Presently, a more compelling theory of cosmology that includes Dark Matter (DM) in order
202 to explain a variety of observations is Λ Cold Dark Matter, or Λ CDM. I present the evidence
203 supporting Λ CDM in Section 2.3 yet discuss the conclusions of the Λ CDM model here. According
204 to Λ CDM fit to observations on the Cosmic Microwave Background (CMB), DM is 26.8% of the
205 universe's current energy budget. Baryonic matter, stuff like atoms, gas, and stars, contributes to
206 4.9% of the universe's current energy budget [1, 2, 3].

207 DM is dark; it does not interact readily with light at any wavelength. DM also does not interact
208 noticeably with the other standard model forces (Strong and Weak) at a rate that is readily observed
209 [3]. DM is cold, which is to say that the average velocity of DM is below relativistic speeds [1].
210 'Hot' DM would not likely manifest the dense structures we observe like galaxies, and instead
211 would produce much more diffuse galaxies than what is observed [3, 1]. DM is old; it played a
212 critical role in the formation of the universe and the structures within it [1, 2].

213 Observations of DM have so far been only gravitational. The parameter space available to what
214 DM could be therefore is extremely broad. The broad DM parameter space is iteratively tested in

215 DM searches by supposing a hypothesis that has not yet been ruled out and performing observations
216 to test them. When the observations yield a null result, the parameter space is constrained further.
217 I present some approaches for DM searches in Section 2.4.

218 **2.3 Evidence for Dark Matter**

219 Dark Matter (DM) has been a looming problem in physics for almost 100 years. Anomalies
220 have been observed by astrophysicists in galactic dynamics as early as 1933 when Fritz Zwicky
221 noticed unusually large velocity dispersion in the Coma cluster. Zwicky's measurement was the
222 first recorded to use the Virial theorem to measure the mass fraction of visible and invisible matter
223 in celestial bodies [4]. From Zwicky in [5], "*If this would be confirmed, we would get the surprising*
224 *result that dark matter is present in much greater amount than luminous matter.*" Zwicky's and
225 others' observation did not instigate a crisis in astrophysics because the measurements did not
226 entirely conflict with their understanding of galaxies [4]. In 1978, Rubin, Ford, and Norbert
227 measured rotation curves for ten spiral galaxies [6]. Rubin et al.'s 1978 publication presented a
228 major challenge to the conventional understanding of galaxies that could no longer be dismissed by
229 measurement uncertainties. Evidence has been mounting ever since for this exotic form of matter.
230 The following subsections provide three compelling pieces of evidence in support of the existence
231 of DM.

232 **2.3.1 First Clues: Stellar Velocities**

233 Zwicky, and later Rubin, measured the stellar velocities of various galaxies to estimate their
234 virial mass. The Virial Theorem upon which these observations are interpreted is written as

$$2T + V = 0. \quad (2.1)$$

235 Where T is the kinetic energy and V is the potential energy in a self-gravitating system. The
236 classical Newton's law of gravity from stars and gas was used for gravitational potential modeled in
237 the observed galaxies:

$$V = -\frac{1}{2} \sum_i \sum_{j \neq i} \frac{m_i m_j}{r_{ij}}. \quad (2.2)$$

238 Zwicky et al. measured just the velocities of stars apparent in optical wavelengths [5]. Rubin et al.
 239 added by measuring the velocity of the hydrogen gas via the 21 cm emission line of Hydrogen [6].
 240 The velocities of the stars and gas are used to infer the total mass of galaxies and galaxy clusters
 241 via Equation (2.1). An inferred mass is obtained from the luminosity of the selected sources. The
 242 two inferences are compared to each other as a luminosity to mass ratio which typically yielded [1]

$$\frac{M}{L} \sim 400 \frac{M_{\odot}}{L_{\odot}} \quad (2.3)$$

243 M_{\odot} and L_{\odot} referring to stellar mass and stellar luminosity, respectively. These ratios clearly indicate
 244 a discrepancy in apparent light and mass from stars and gas and their velocities.

245 Rubin et al. [6] demonstrated that the discrepancy was unlikely to be an underestimation of
 246 the mass of the stars and gas. The inferred "dark" mass was up to 5 times more than the luminous
 247 mass. This dark mass also needed to extend well beyond the extent of the luminous matter.

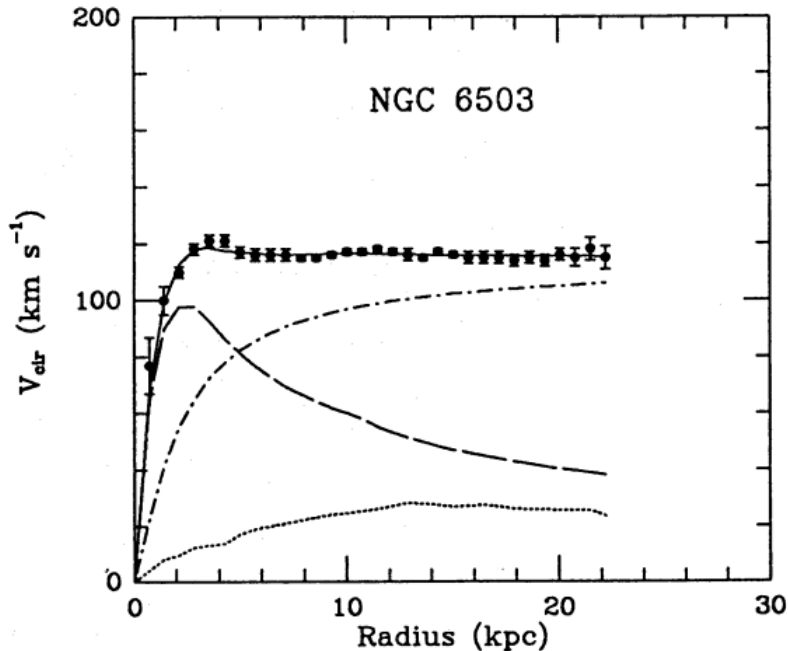


Figure 2.1 Rotation curve fit to NGC 6503 from [7]. Dashed line is the contribution from visible matter. Dotted curves are from gas. Dash-dot curves are from dark matter (DM). Solid line is the composite contribution from all matter and DM sources. Data are indicated with bold dots with error bars. Data agree strongly with a matter + DM composite prediction.

248 Figure 2.1 features one of many rotation curves plotted from the stellar velocities within galaxies.

249 The measured rotation curves mostly feature a flattening of velocities at higher radius which is not
250 expected if the gravity was only coming from gas and luminous matter. The extension of the
251 flat velocity region also indicates that the DM is distributed far from the center of the galaxy.
252 Modern velocity measurements include significantly larger objects, galactic clusters, and smaller
253 objects, dwarf galaxies. Yet, measurements along this regime are leveraging the Virial theorem
254 with Newtonian potential energies. We know Newtonian gravity is not a comprehensive description
255 of gravity. New observational techniques have been developed since 1978, and those are discussed
256 in the following sections.

257 **2.3.2 Evidence for Dark Matter: Gravitational Lensing**

258 Modern evidence for dark matter comes from new avenues beyond stellar velocities. Grav-
259 itational lensing from DM is a new channel from general relativity. General relativity predicts
260 aberrations in light caused by massive objects. In recent decades we have been able to measure the
261 lensing effects from compact objects and DM halos. Figure 2.2 shows how different massive ob-
262 jects change the final image of a faraway galaxy resulting from gravitational lensing. Gravitational
263 lensing developed our understanding of dark matter in two important ways.

264 Gravitational lensing provides additional compelling evidence for DM. The observation of two
265 merging galactic clusters in 2006, shown in Figure 2.3, provided a compelling argument for DM
266 outside the Standard Model. These clusters merged recently in astrophysical time scales. Galaxies
267 and star cluster have mostly passed by each other as the likelihood of their collision is low. Therefore,
268 these massive objects will mostly track the highest mass, dark and/or baryonic, density. Yet, the
269 intergalactic gas is responsible for the majority of the baryonic mass in the systems [4]. These gas
270 bodies will not phase through and will heat up as they collide together. The hot gas is located via
271 x-ray emission from the cluster. Two observations of the clusters were performed independently of
272 each other.

273 The first was the lensing of light around the galaxies due to their gravitational influences.
274 When celestial bodies are large enough, the gravity they exert bends space and time itself. The
275 warped space-time lenses light and will deflect in an analogous way to how glass lenses will bend

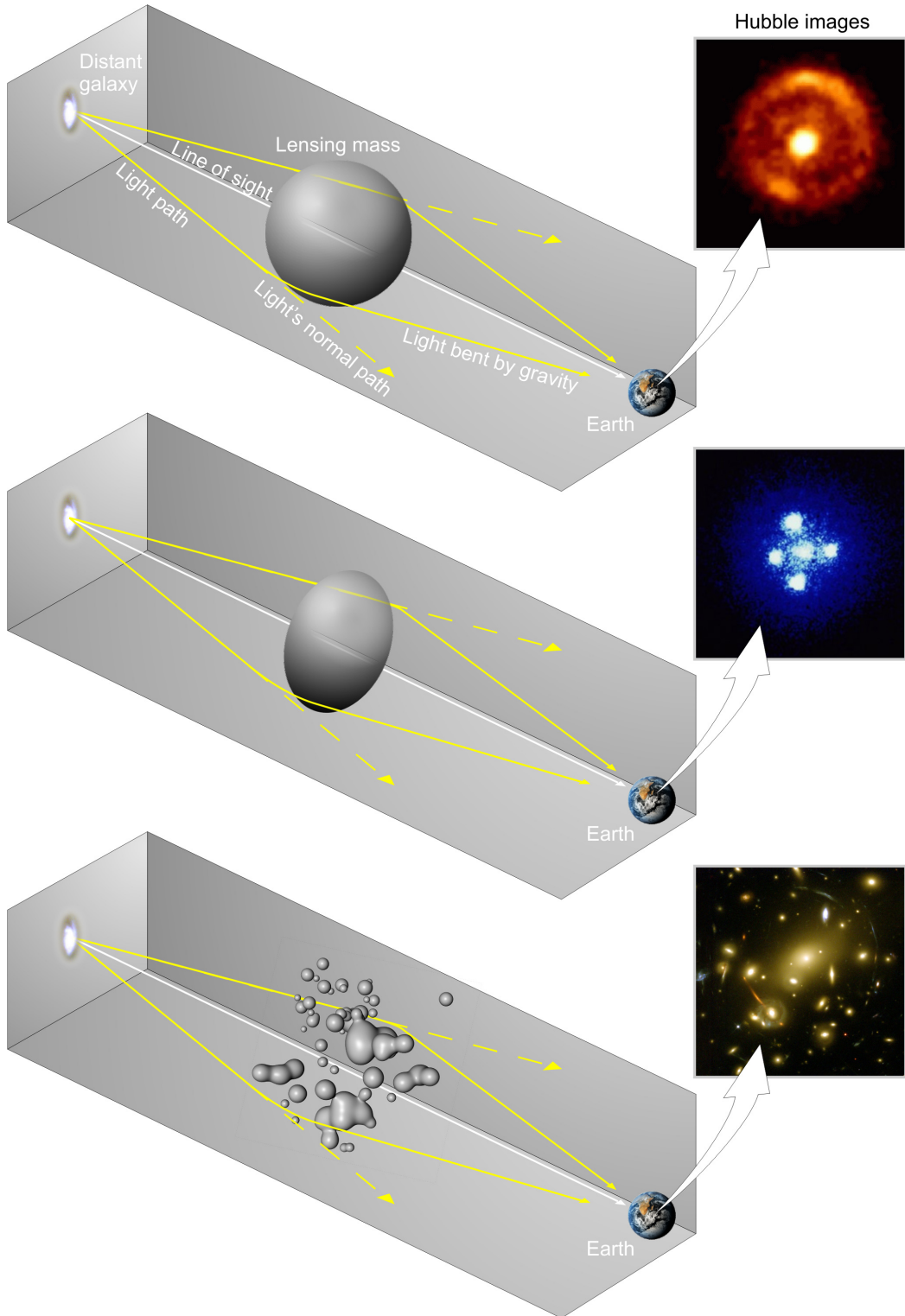


Figure 2.2 Light from distant galaxy is bent in unique ways depending on the distribution of mass between the galaxy and Earth. Yellow dashed lines indicate where the light would have gone if the matter were not present [8].

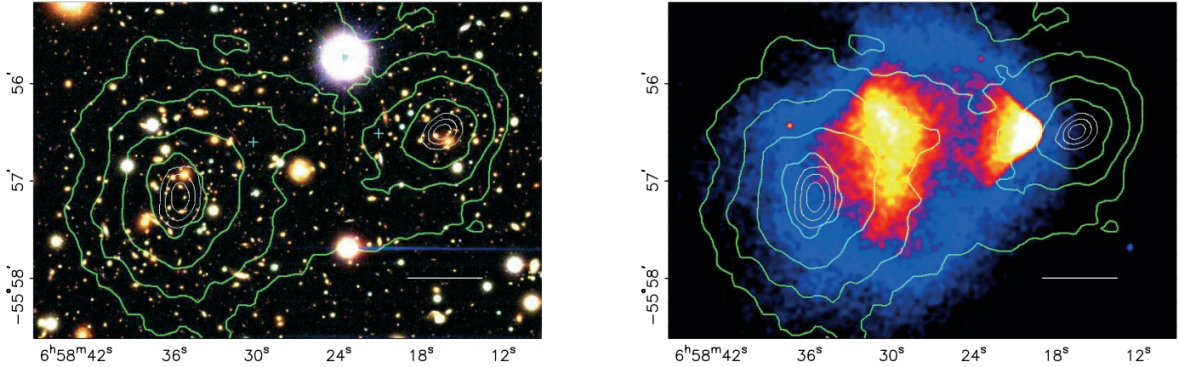


Figure 2.3 (left) Optical image of galactic cluster 1E0657-558. (right) X-ray image of the cluster with redder meaning hotter and higher baryon density. (both) Green contours are reconstruction of gravity contours from weak lensing. White rings are the best fit mass maxima at 68.3%, 95.5%, and 99.7% confidence. The matter maxima of the clusters are clearly separated from x-ray maxima. [9]

276 light, see Figure 2.2. With a sufficient understanding of light sources behind a massive object, we
 277 can reconstruct the contours of the gravitational lenses. The gradient of the contours shown in
 278 Figure 2.3 then indicates how dense the matter is and where it is.

279 The x-ray emission can then be observed from the clusters. Since these galaxies are mostly gas
 280 and are merging, then the gas should be getting hotter. If they are merging, the x-ray emissions
 281 should be the strongest where the gas is mostly moving through each other. Hence, X-ray emission
 282 maps out where the gas is in the merging galaxy cluster.

283 The lensing and x-ray observations were done on the Bullet cluster featured on Figure 2.3.
 284 The x-ray emissions do not align with the gravitational contours from lensing. The incongruence
 285 in mass density and baryon density suggests that there is a lot of matter somewhere that does
 286 not interact with light. Moreover, this dark matter cannot be baryonic [9]. The Bullet Cluster
 287 measurement did not really tell us what DM is exactly, but it did give the clue that DM also does
 288 not interact with itself very strongly. If DM did interact strongly with itself, then it would have been
 289 more aligned with the x-ray emission [9]. There have been follow-up studies of galaxy clusters with
 290 similar results. The Bullet Cluster and others like it provide a persuasive case against something
 291 possibly amiss in our gravitational theories.

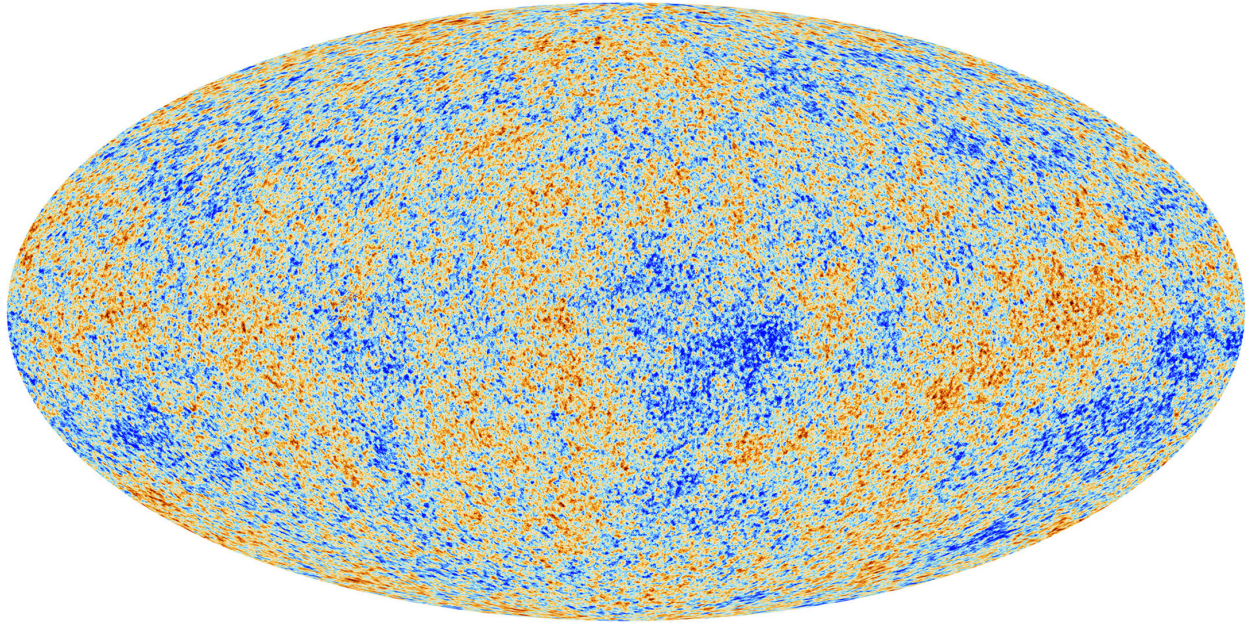


Figure 2.4 Plank CMB sky. Sky map features small variations in temperature in primordial light. These anisotropies are used to make inferences about the universe’s energy budget and developmental history. [10]

292 **2.3.3 Evidence for Dark Matter: Cosmic Microwave Background**

293 The Cosmic Microwave Background (CMB) is the primordial light from the early universe
294 when Hydrogen atoms formed from the free electron and proton soup in the early universe. The
295 CMB is the earliest light we can observe; released when the universe was about 380,000 years old.
296 Then we look at how the simulated universes look like compared to what we see. Figure 2.4 is the
297 most recent CMB image from the Plank satellite after subtracting the average value and masking the
298 galactic plane [10]. Redder regions indicate a slightly hotter region in the CMB, and blue indicates
299 colder. The intensity variations are on the order of 1 in 1000 with respect to the average value.

300 The Cosmic Microwave Background shows that the universe had DM in it from an incredibly
301 early stage. To measure the DM, Dark Energy, and matter fractions of the universe from the CMB,
302 the image is analyzed into a power spectrum, which shows the amplitude of the fluctuations as
303 a function of spherical multipole moments. Λ CDM provides the best fit to the power spectra of
304 the CMB as shown in Figure 2.5. The CMB power spectrum is quite sensitive to the fraction
305 of each energy contribution in the early universe. Low l modes are dominated by variations
306 in gravitational potential. Intermediate l emerge from oscillations in photon-baryon fluid from

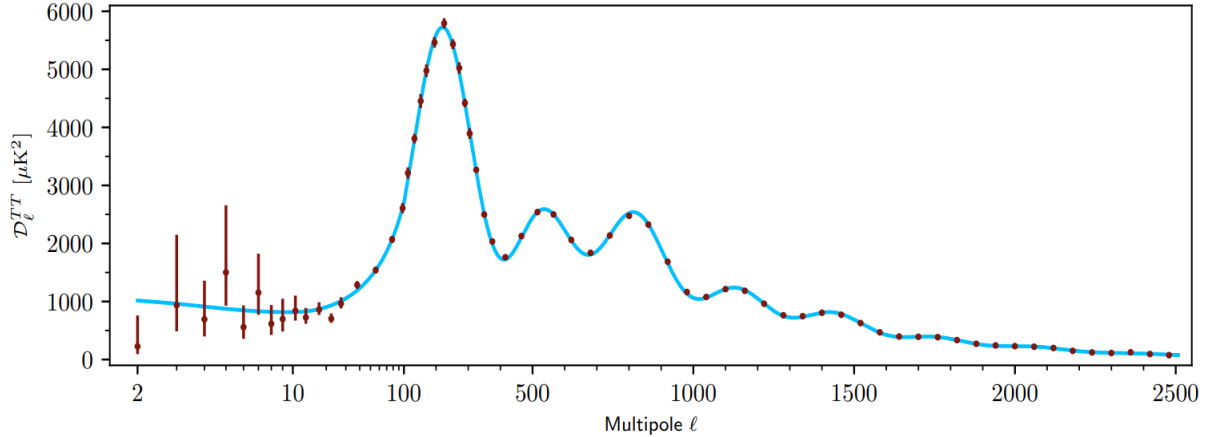


Figure 2.5 Observed Cosmic Microwave Background power spectrum as a function of multipole moment from Plank [10]. Blue line is best fit model from Λ CDM. Red points and lines are data and error, respectively.

307 competing baryon pressures and gravity. High l is a damped region from the diffusion of photons
 308 during electron-proton recombination. [1]

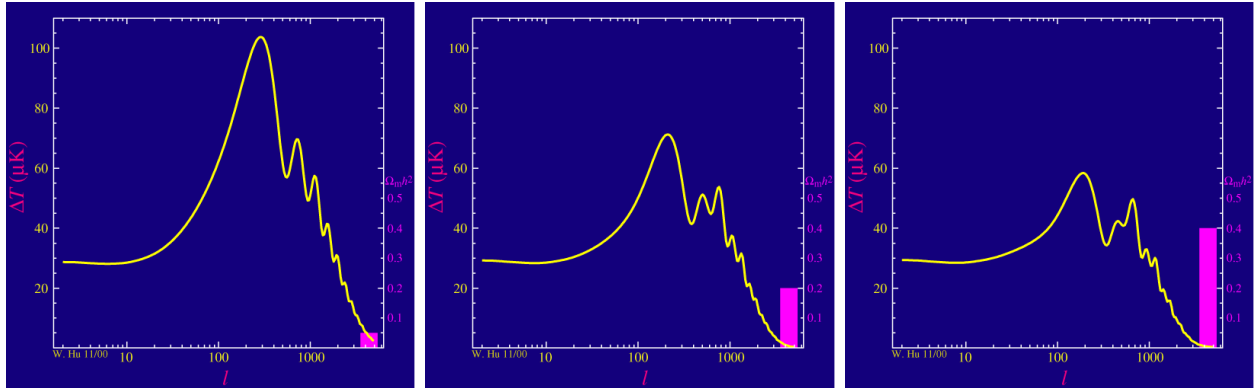


Figure 2.6 Predicted power spectra of CMB for different $\Omega_m h^2$ values for fixed baryon density from [11]. (left) Low $\Omega_m h^2$ increases the prominence of first and second peaks. (middle) $\Omega_m h^2$ is most similar to the observed power spectrum. The second and third peaks are similar in height. (right) $\Omega_m h^2$ is large which suppresses the first peak and raises the prominence of the third peak.

309 The harmonics would look quite different for a universe with less DM. Figure 2.6 demonstrates
 310 the effect $\Omega_m h^2$ has on the expected power spectrum for fixed baryon matter density. [11] Sweeping
 311 $\Omega_m h^2$ in this way clearly shows the effect dark matter has on the CMB power spectrum. The
 312 observations fit well with the Λ CDM model, and the derived fractions are as follows. The matter
 313 fraction: $\Omega_m = 0.3153$; and the baryon fraction: $\Omega_b = 0.04936$ [10]. Plank's observations also
 314 provide a measure of the Hubble constant, H_0 . H_0 especially has seen a growing tension in the

315 past decade that continues to deepened with observations from instruments like the James Webb
316 Telescope [12, 13]. As Hubble tensions deepen, we may find that perhaps Λ **CDM**, despite its
317 successes, is missing some critical physics.

318 Overall, the Newtonian motion of stars in galaxies, weak lensing from galactic clusters, and
319 power spectra from primordial light form a compelling body of research in favor of dark matter.
320 It takes another leap of theory and experimentation to make observations of DM that are non-
321 gravitational in nature. In Section 2.3, the evidence for DM implies strongly that the DM is matter
322 and not a lost parameter in the gravitational fields between massive objects. Finally, if we take one
323 axiom: that this matter has quantum behavior, such as being described by some Bohr wavelength
324 and abiding by some fermion or boson statistics; then we arrive at particle dark matter. One particle
325 DM hypothesis is the Weakly Interacting Massive Particle (WIMP). This DM candidate theory is
326 discussed further in the next section and is the focus of this thesis.

327 **2.4 Searching for Dark Matter: Particle DM**

328 Section 2.4 shows the Standard Model of particle physics and is currently the most accurate
329 model for the dynamics of fundamental particles like electrons and photons. The current status
330 of the SM does not have a viable DM candidate. When looking at the standard model, we can
331 immediately exclude any charged particle because charged particles interact strongly with light.
332 Specifically, this will rule out the following charged, fundamental particles: $e, \mu, \tau, W, u, d, s, c, t, b$
333 and their corresponding antiparticles. Recalling from Section 2.2 that DM must be long-lived and
334 stable over the age of the universe which excludes all SM particles with decay half-lives at or shorter
335 than the age of the universe. The lifetime constraint additionally eliminates the Z and H bosons.
336 Finally, the candidate DM needs to be somewhat massive. Recall from Section 2.2 that DM is cold
337 or not relativistic through the universe. This eliminates the remaining SM particles: $\nu_{e,\mu,\tau}, g, \gamma$ as
338 DM candidates. Because there are no DM candidates within the SM, the DM problem strongly
339 hints to physics beyond the SM (BSM).

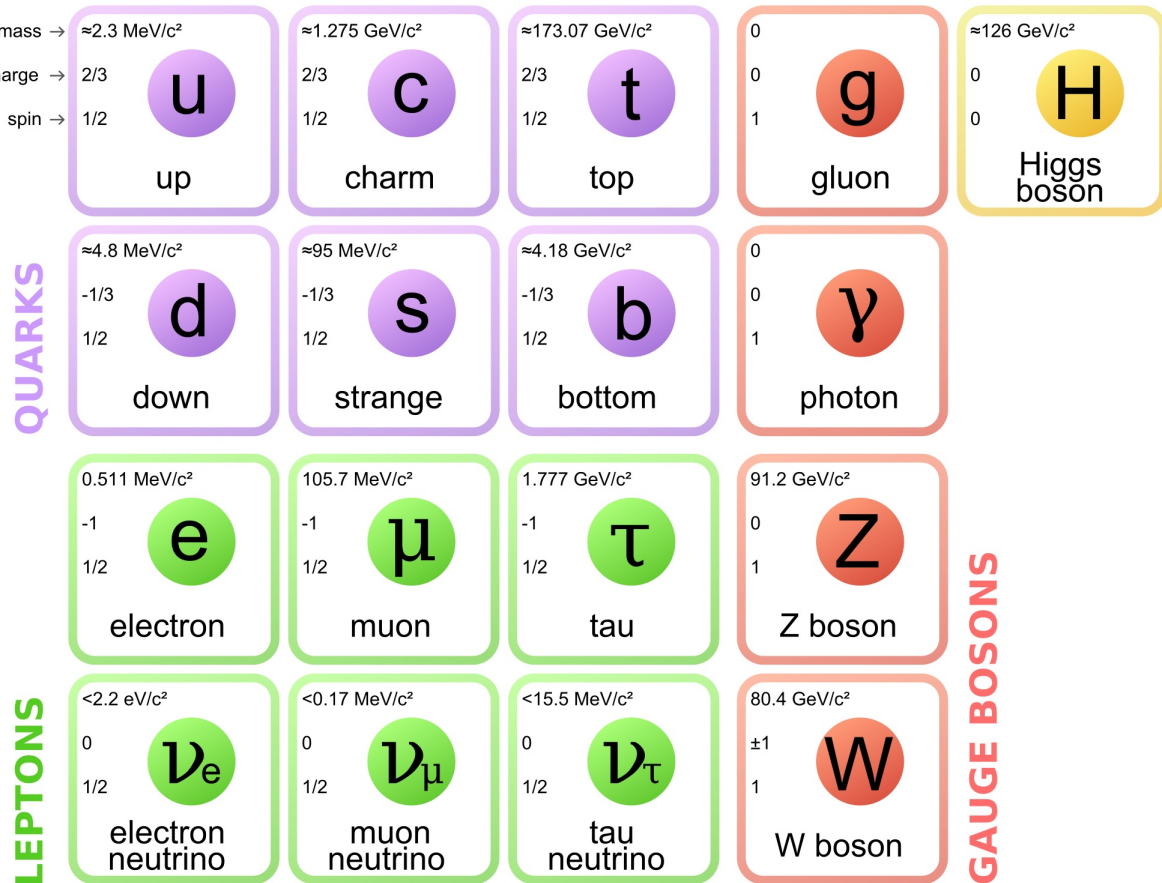


Figure 2.7 The Standard Model (SM) of particle physics. Figure taken from <http://www.quantumdiaries.org/2014/03/14/the-standard-model-a-beautiful-but-flawed-theory/>

340 2.4.1 Shake it, Break it, Make it

341 When considering DM that couples in some way with the SM, the interactions are roughly
 342 demonstrated by interaction demonstrated in Figure 2.8. The figure is a simplified Feynman
 343 diagram where the arrow of time represents the interaction modes of: **Shake it, Break it, Make it.**

344 **Shake it** refers to the direct detection of dark matter. Direct detection interactions start with
 345 a free DM particle and an SM particle. The DM and SM interact via elastic or inelastic collision
 346 and recoil away from each other. The DM remains in the dark sector and imparts some momentum
 347 onto the SM particle. The hope is that the momentum imparted onto the SM particle is sufficiently
 348 high enough to pick up with extremely sensitive instruments. Because we cannot create the DM in
 349 the lab, a direct detection experiment must wait until DM is incident on the detector. Most direct
 350 detection experiments are therefore placed in low-background environments with inert detection

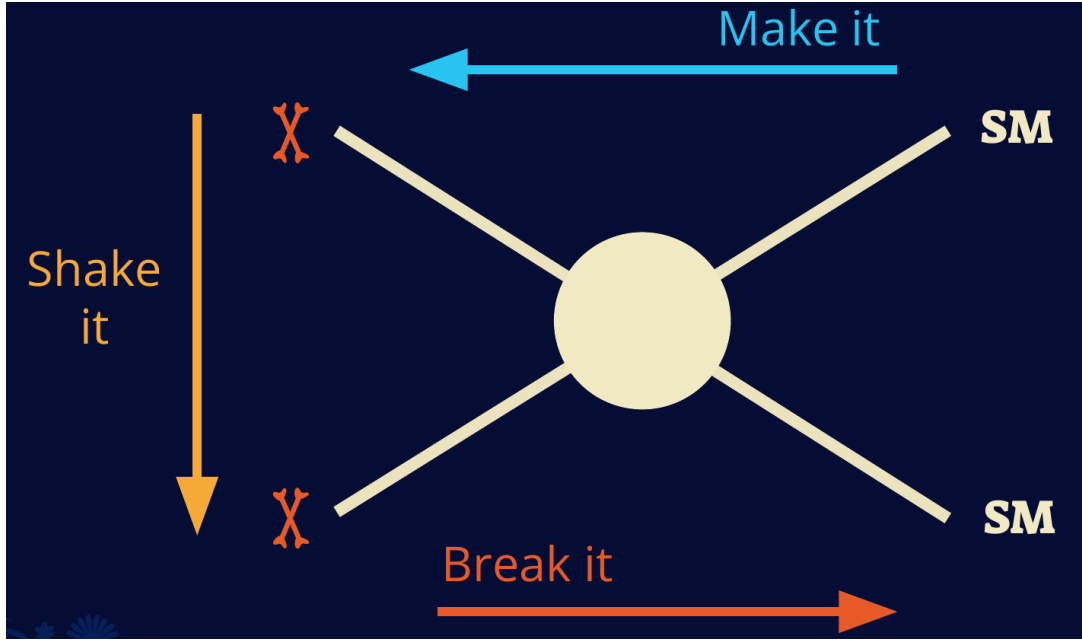


Figure 2.8 Simplified Feynman diagram demonstrating different ways DM can interact with SM particles. The 'X's refer to the DM particles whereas the SM refer to fundamental particles in the SM. The large circle in the center indicates the vertex of interaction and is purposely left vague. The colored arrows refer to different directions of time as well as their respective labels. The arrows indicate the initial and final state of the DM -SM interaction in time.

³⁵¹ media like the noble gas Xenon. [14]

³⁵² **Make it** refers to the production of DM from SM initial states. The experiment starts with
³⁵³ particles in the SM. These SM particles are accelerated to incredibly high energies and then collide
³⁵⁴ with each other. In the confluence of energy, DM hopefully emerges as a byproduct of the SM
³⁵⁵ annihilation. Often it is the collider experiments that are energetic enough to hypothetically produce
³⁵⁶ DM. These experiments include the world-wide collaborations ATLAS and CMS at CERN where
³⁵⁷ proton collide together at extreme energies. The DM searches, however, are complex. DM likely
³⁵⁸ does not interact with the detectors and lives long enough to escape the detection apparatus of
³⁵⁹ CERN's colliders. This means any DM production experiment searches for an excess of events
³⁶⁰ with missing momentum or energy in the events. An example event with missing transverse
³⁶¹ momentum is shown in Figure 2.9. The missing momentum with no particle tracks implies a
³⁶² neutral particle carried the energy out of the detector. However, there are other neutral particles
³⁶³ in the SM, like neutrons or neutrinos, so any analysis has to account for SM signatures of missing

364 momentum. [15]

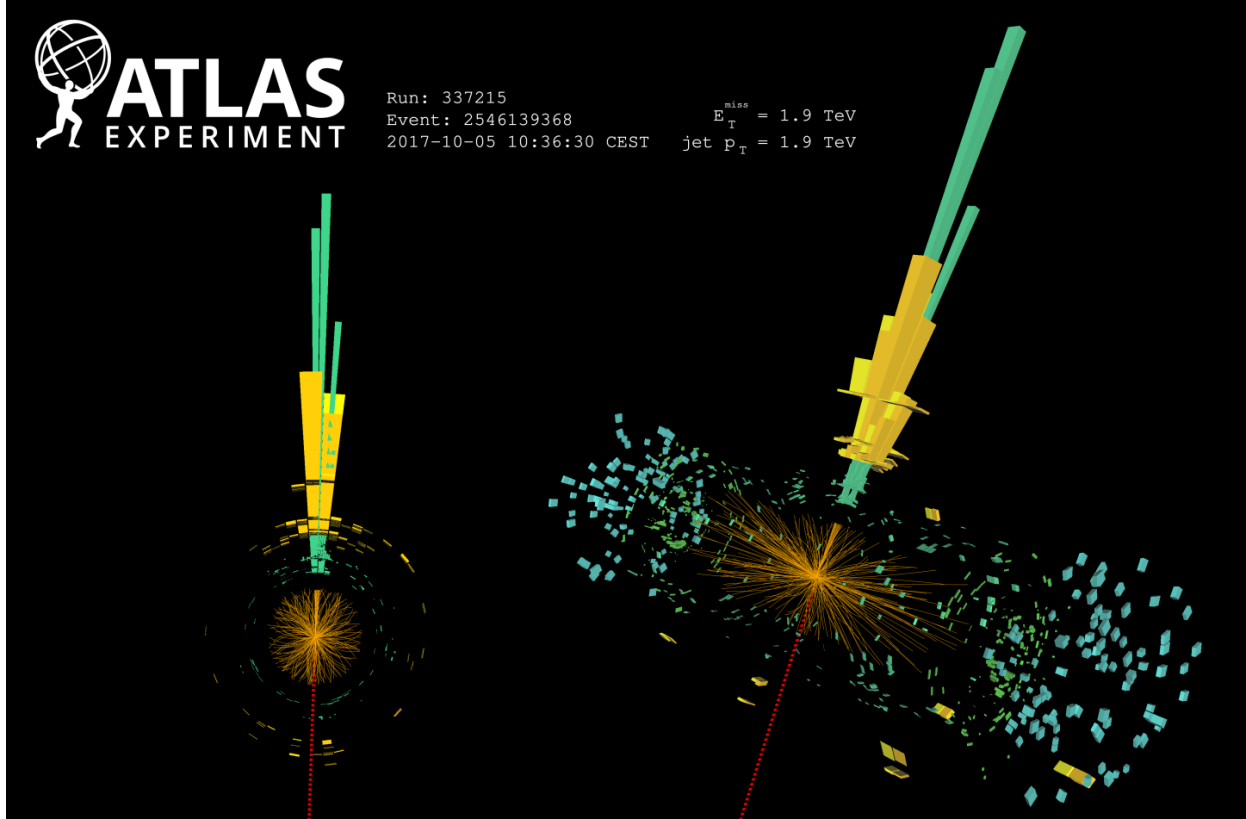


Figure 2.9 A single jet event in ATLAS detector from 2017 [16]. Jet momentum was observed to be 1.9 TeV. Missing transverse momentum was observed to be 1.9 TeV compared to the initial transverse momentum of the event was 0. Implied MET is traced by a red dashed line in event display.

365 2.4.2 Break it: Standard Model Signatures of Dark Matter through Indirect Searches

366 **Break it** refers to the creation of SM particles from the dark sector, and it is the primary focus
367 of this thesis. The interaction begins with DM or in the dark sector. The hypothesis is that this
368 DM will either annihilate with itself or decay and produce an SM byproduct. This method is
369 often referred to as the Indirect Detection of DM because we have no lab to directly control or
370 manipulate the DM. Therefore, most indirect DM searches are performed using observations of
371 known DM densities among the astrophysical sources. The strength is that we have the whole of the
372 universe and its 13.6-billion-year lifespan to use as a detector and particle accelerator. Additionally,
373 locations of dark matter are well cataloged since it was astrophysical observations that presented

374 the problem of DM in the first place.

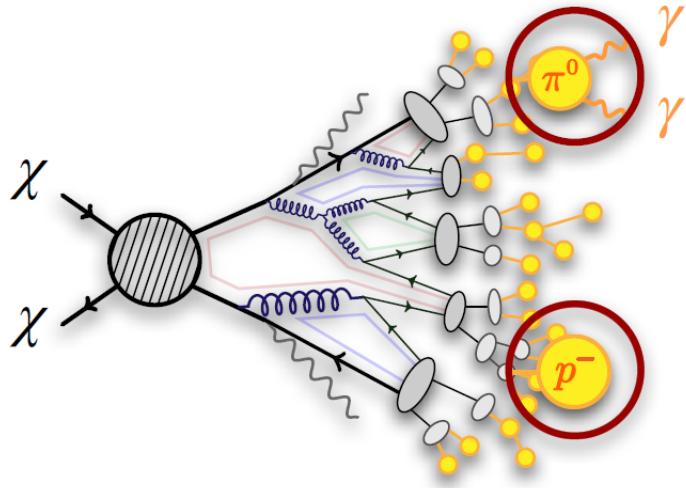


Figure 2.10 More detailed pseudo-Feynman diagram of particle cascade from dark matter annihilation into 2 quarks. The quarks hadronize and down to stable particles like γ or the anti-proton (p^-). Diagram pulled from ICRC 2021 presentation on DM annihilation search [17].

375 However, anything can happen in the universe. There are many difficult to deconvolve back-
376 grounds when searching for DM. One prominent example is the galactic center. We know the
377 galactic center has a large DM content because of stellar kinematics in our Milky Way and DM halo
378 simulations. Yet, any signal from the galactic center is challenging to parse apart from the extreme
379 environment of our supermassive black hole, unresolved sources, and diffuse emission from the
380 interstellar medium [18]. Despite the challenges, any DM model that yields evidence in the other
381 two observation methods, **Shake it or Make it** must be corroborated with indirect observations of
382 the known DM sources. Without corroborating evidence, DM observation in the lab is hard-pressed
383 to demonstrate that it is the model contributing to the DM seen at the universal scale.

384 In the case of WIMP DM, signals are described in terms of primary SM particles produced
385 from DM decay or annihilation. The SM initial state particles are then simulated down to stable
386 final states such as the γ , ν , p , or e which can traverse galactic lengths to reach Earth.

387 Figure 2.10 shows the quagmire of SM particles that emerges from SM initial states that are not
388 stable [17]. There are many SM particles with varying energies that can be produced in such an

389 interaction. For any arbitrary DM source and stable SM particle, the SM flux from DM annihilating
 390 to a neutral particle in the SM, ϕ , from a region in the sky is described by the following.

$$\frac{d\Phi_\phi}{dE_\phi} = \frac{\langle\sigma v\rangle}{8\pi m_\chi^2} \frac{dN_\phi}{dE_\phi} \times \int_{\text{source}} d\Omega \int_{l.o.s} \rho_\chi^2 dl(r, \theta') \quad (2.4)$$

391 In Equation (7.1), $\langle\sigma v\rangle$ is the velocity-weighted annihilation cross-section of DM to the SM. m_χ
 392 refers to the mass of DM, noted with Greek letter χ . $\frac{dN_\phi}{dE_\phi}$ is the N particle flux weighted by the
 393 particle energy. An example is provided in Figure 2.11 for the γ final state. The integrated terms
 394 are performed over the solid angle, $d\Omega$, and line of sight, l.o.s. ρ is the density of DM for a
 395 location (r, θ') in the sky. The terms left of the ' \times ' are often referred to as the particle physics
 396 component. The terms on the right are referred to as the astrophysical component. For decaying
 397 DM, the equation changes to...

$$\frac{d\Phi_\phi}{dE_\phi} = \frac{1}{4\pi\tau m_\chi} \frac{dN_\phi}{dE_\phi} \times \int_{\text{source}} d\Omega \int_{l.o.s} \rho_\chi dl(r, \theta') \quad (2.5)$$

398 In Equation (2.5), τ is the decay lifetime of the DM. Just as in Equation (7.1), the left and
 399 right terms are the particle physics and the astrophysical components respectively. The integrated
 400 astrophysical component of Equation (7.1) is often called the J-Factor. Whereas the integrated
 401 astrophysical component of Equation (2.5) is often called the D-Factor.

402 Exact DM $\text{DM} \rightarrow \text{SM SM}$ branching ratios are not known, so it is usually assumed to go 100%
 403 into an SM particle/anti-particle. Additionally, when a DM annihilation or decay produces one of
 404 the neutral, long-lived SM particles (ν or γ), the particle is traced back to a DM source. For DM
 405 above GeV energies, there are very few SM processes that can produce particles with such a high
 406 energy. Seeing such a signal would almost certainly be an indication of the presence of dark matter.
 407 Fortunately, the universe provides us with the largest volume and lifetime ever for a particle physics
 408 experiment.

409 2.5 Sources for Indirect Dark Matter Searches

410 The first detection of DM relied on optical observations. Since then, we have developed new
 411 techniques to find DM dense regions. As described in Section 2.3.1, many DM dense regions were
 412 through observing galactic rotation curves. Our Milky Way galaxy is among DM dense regions

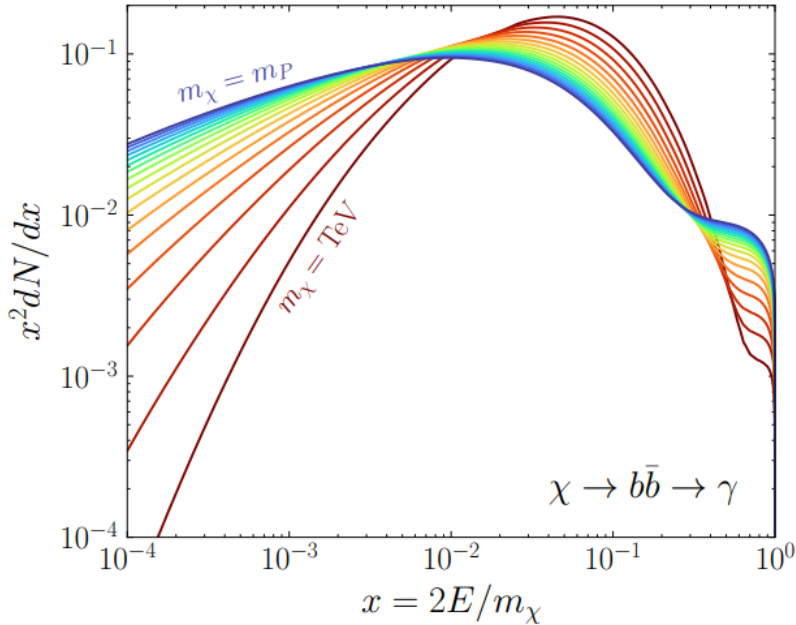


Figure 2.11 Dark Matter (DM) decay spectrum for $b\bar{b}$ initial state and γ final state. Redder spectra are for larger DM masses. Bluer spectra are light DM masses. x is a unitless factor defined as the ratio of the mass of DM, m_χ , and the final state particle energy E_γ . Figure from [19].

discovered, and it is the largest nearby DM dense region to look at. Additionally, the DM halo surrounding the Milky Way is clumpy [18]. There are regions in the DM halo of the Milky Way that have more DM than others that have captured gas over time. These sub-halos were dense enough to collapse gas and form stars. These apparent sub galaxies are known as dwarf spheroidal galaxies and are the main sources studied in this thesis. Each source type comes with different trade-offs. Galactic Center studies will be very sensitive to the assumed distribution of DM. The central DM density can vary substantially as demonstrated in Figure 2.12. At distances close to the center of the galaxy, or small r , the differences in DM densities can be 3-4 orders of magnitude. Searches toward the galactic center will therefore be quite sensitive to the assumed DM distribution.

Searches toward Dwarf Spheroidal Galaxies (dSph's) suffer from uncertainties in the DM density less than the galactic center studies. This is mostly from their diminutive size being smaller than the angular resolution of most γ -ray observatories [18]. The DM content dSph's are typically determined with the Virial theorem, Equation (2.1), and are usually majority DM [18] in mass. DSph's tend to be ideal sources to look at for DM searches. Their environments are quiet with little

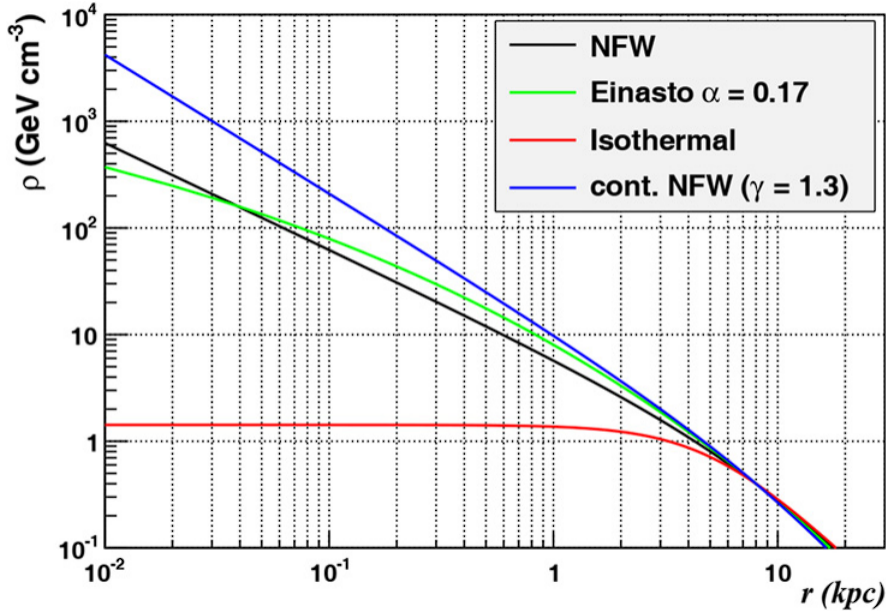


Figure 2.12 Different dark matter density profiles compared. Some models produce exceptionally large densities at small r [20].

427 astrophysical background. Unlike the galactic center, the most active components of dSph's are the
 428 stars within them versus a violent accretion disc around a black hole. All this together means that
 429 dSph's are among the best sources to look at for indirect DM searches. dSph's are the targets of
 430 focus for this thesis.

431 2.6 Multi-Messenger Dark Matter

432 Astrophysics entered a new phase in the past few decades that leverages our increasing sensitivity
 433 to SM channels and general relativity (GR). Up until the 21st century, astrophysical observations
 434 were performed with photons (γ) only. Astrophysics with this 'messenger' is fairly mature now.
 435 Novel observations of the universe have since only adjusted the sensitivity of the wavelength of
 436 light that is observed except at MeV energies. Gems like the CMB [10], and more have ultimately
 437 been observations of different wavelengths of light. Multi-messenger astrophysics proposes using
 438 other SM particles such the $p^{+/-}$, or ν or gravitation waves predicted by general relativity.

439 The experiment LIGO had a revolutionary discovery in 2016 with the first detection of a binary
 440 black hole merger [21]. This opened the collective imagination to observing the universe through
 441 gravitational waves. There has also been a surge of interest in the neutrino (ν) sector. IceCube

442 demonstrated that we are sensitive to neutrinos in regions that correlate with significant photon
 443 emission like the galactic plane [22]. Neutrinos, like gravitational waves and light, travel mostly
 444 unimpeded from their source to our observatories. This makes pointing to the originating source
 445 of these messengers much easier than it is for cosmic rays which are deflected from their source by
 446 magnetic fields.

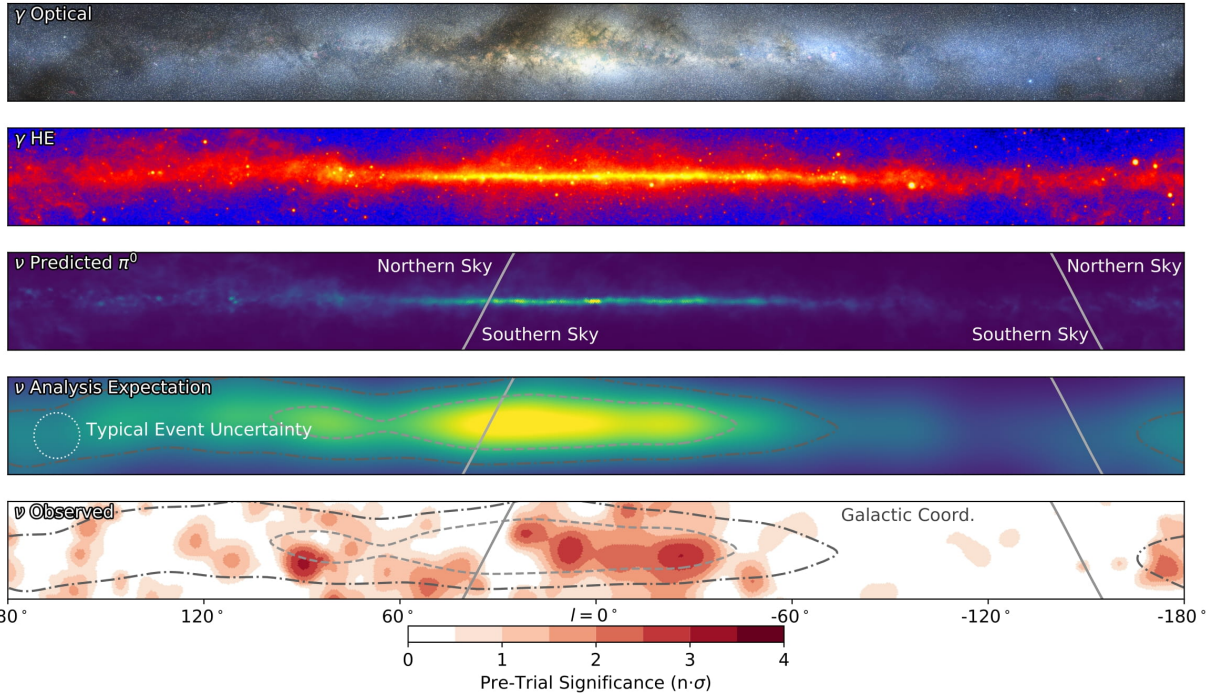


Figure 2.13 The Milky Way Galaxy in photons (γ) and neutrinos (ν) [22]. The Galactic center is at $l=0^\circ$ and is the brightest region in all panels. (top) An Optical color image of the Milky Way galaxy seen from Earth. Clouds of gas and dust obscure some light from stars. (2nd down) Integrated flux of γ -rays observed by the Fermi-LAT telescope [23]. (middle) Expected neutrino emission that corresponds with Fermi-LAT observations. (2nd up) Expected neutrino emission profile after considering detector systematics of IceCube. (bottom) Observed neutrino emission from region of the galactic plane. Substantial neutrino emission was detected.

447 The IceCube collaboration recently published a groundbreaking result of the Milky Way in
 448 neutrinos. The recent result from IceCube, shown in Figure 2.13, proves that we can make
 449 observations under different messenger regimes. The top two panels show the appearance of the
 450 galactic plane to different wavelengths of light. Some sources are more apparent in some panels,
 451 while others are not. This new channel is powerful because neutrinos are readily able to penetrate
 452 through gas and dust in the Milky Way. This new image also refines our understanding of how high

453 energy particles are produced. For example, the fit to IceCube data prefers neutrino production
 454 from the decay of π^0 [22].

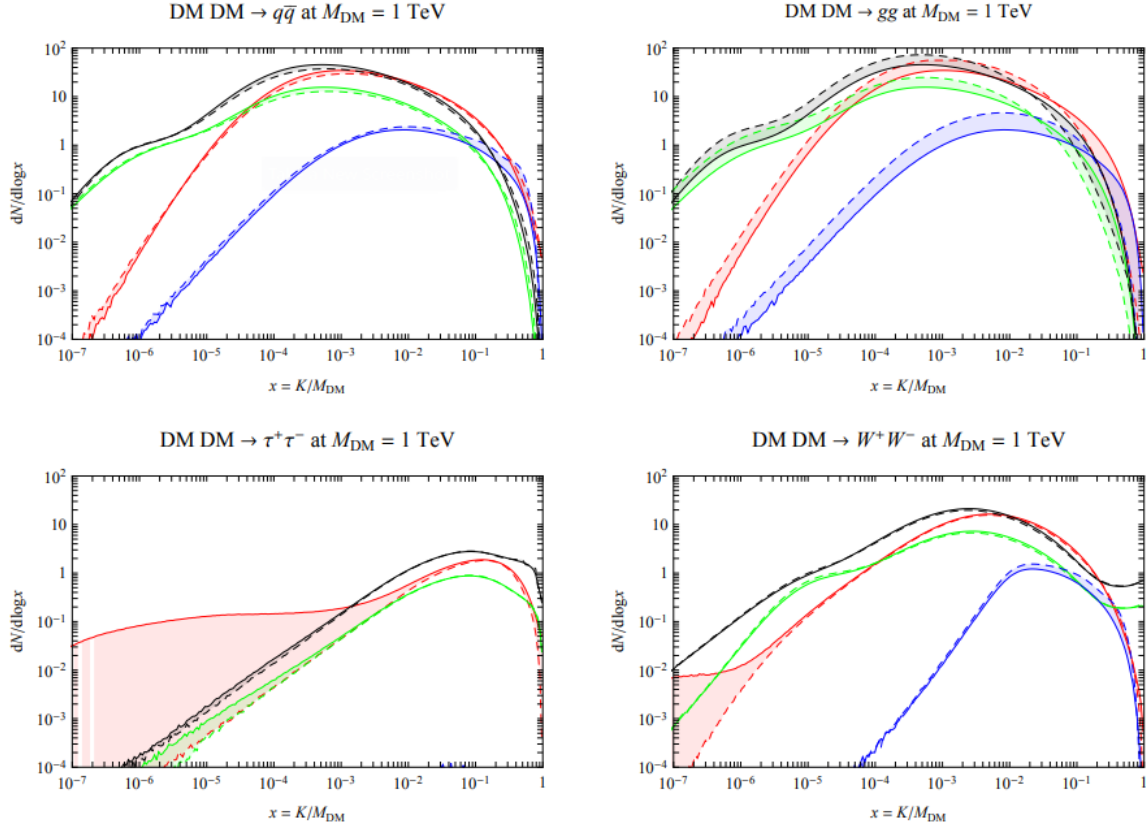


Figure 2.14 Dark Matter annihilation spectra for different final state particle and standard model annihilation channels [24]. Photons (red), e^\pm (green), \bar{p} (blue), ν (black).

455 Exposing our observations to more cosmic messengers greatly increases our sensitivity to
 456 rare processes. In the case of DM, Figure 2.14, there are many SM particles produced in DM
 457 annihilation. Among the final state fluxes are gammas and neutrinos. Charged particles are also
 458 produced however they would not likely make it to Earth since they will be deflected by magnetic
 459 fields between the source and Earth. This means observatories that can see the neutral messengers
 460 are especially good for DM searches and for combining data for a multi-messenger DM search.

CHAPTER 3

461 **MULTIMESSENGER ASTROPHYSICS: DETECTING HIGH ENERGY NEUTRAL** 462 **MESSENGERS**

463 **3.1 Introduction**

464 Before the 20th century, all asttrophysics observations were optical in nature. We litterly only
465 saw things with highly magnified optical observations. Then we discovered cosmic rays. cosmic
466 rays are charged particles, typically naked protons or H+. This was seen by Victor Hess in 19??.
467 Around the same time we discovered neutrinos from beta decay. Sometime around 1950 we started
468 to build neutrino detectors which were mostly sensitive to neutrinos from the sun. Finally, it was
469 theorized that compact objects like black holes and neutron stars would create waves in space-time
470 when they experience mergers or collisions.

471 In the 21st century, we have developed new observation techniques and detectors that are no only
472 sensitive to these four messengers - photons (**TODO: photon**), neutrinos (**TODO: nu**), Cosmic
473 Rays (CR), and Gravitational Wave (WV) - we're collect high energy versions of these events.
474 For the standad model particles, we're now sensitive to all messengers above the MeV eneryg
475 range. Additionally, the GW's were sensitive to are in the stellar mass black hole region and above
476 within our galactic neighborhood. This means were becoming sensitive to the fundamental physics
477 occuring within the universe and we can rely on the universe as a TeV+ particle accelerator. We
478 also have the abaility to correlate high energy events across messengers and gain new insights on
479 the processes that occur in our universe.

480 This thesis focuses on very high energy (VHE) gamma rays and neutrinos. These can both be
481 observed through the water cherenkov detection technique altho not exclusively. Methods on how
482 to detect and observe these neutral messengers are discussed Section 3.3 and Section 3.4

483 **3.2 Charged Particles in a Medium**

484 For high enery gamma-rays and neutrinos, we can exploit the same effect that charged particles
485 have with water. This effect is known as Cherenkov radiation. Cherenkov Radiation occurs when a
486 charged particle, usually electrons (e) or muons (μ), traverse a medium, like water, faster than the

487 speed of light in that medium. This is similar to sonic boom where an object moves through air
488 faster than the speed of sound in air. Cherenkov radiation can therefore be thought of as an 'optic
489 boom'. Many astro-particle physics experiments will use water as the medium as because water
490 has a unique set of properties ideal for charged particle tracking.



Figure 3.1 TODO: Show a nuclear reactor with cherenkov radiation[NEEDS A SOURCE][FACT CHECK THIS]

491 The frequency of light emitted due to cherenkov radiation follows the equation:

$$INSERT\ Cherenkov\ wavelength\ calc\ HERE. \quad (3.1)$$

492 The absorption spectra is shown in the following figure:

493 **3.3 Photons (γ)**

494 **3.4 Neutrinos (ν)**

495 **3.5 Opportunities to Combine for Dark Matter**



Figure 3.2 TODO: absorption spectrum of liquid and solid water[NEEDS A SOURCE][FACT CHECK THIS]

CHAPTER 4

496

HIGH ALTITUDE WATER CHERENKOV (HAWC) OBSERVATORY

497 **4.1 The Detector**

498 **4.2 Events Reconstruction and Data Acquisition**

499 **4.2.1 G/H Discrimination**

500 **4.2.2 Angle**

501 **4.2.3 Energy**

502 **4.3 Remote Monitoring**

503 **4.3.1 ATHENA Database**

504 **4.3.2 HOMER**

505

CHAPTER 5

ICECUBE NEUTRINO OBSERVATORY

506 **5.1 The Detector**

507 **5.2 Events Reconstruction and Data Acquisition**

508 **5.2.1 Angle**

509 **5.2.2 Energy**

510 **5.3 Northern Test Site**

511 **5.3.1 PIgeon remote dark rate testing**

512 **5.3.2 Bulkhead Construction**

CHAPTER 6

COMPUTATIONAL TECHNIQUES IN PARTICLE ASTROPHYSICS

514 **6.1 Neural Networks for Gamma/Hadron Separation**

515 **6.2 Parallel Computing for Dark Matter Analyses**

CHAPTER 7**GLORY DUCK**517 **7.1 Dataset and Background**518 **7.1.1 Data Files**

- 519 • Detector Resolution: `response_aerie_svn_27754_systematics_best_mc_test_no`
 520 `broadpulse_10pctlogchargesmearing_0.63qe_25kHzNoise_run5481_curvatu`
 521 `re0_index3.root`
- 522 • Data Map: `maps-20180119/liff/maptree_1024.root`

523 **7.1.2 Data Set Chosen**

524 The maps used for this analysis contain 1017 days of data between runs 2104 (2014-11-26) and
 525 7476 (2017-12-20). They were generated from pass 4.0 reconstruction. The analysis is performed
 526 using the f_{hit} energy binning scheme with bins [1-9] similar to what was done for the Crab and
 527 previous HAWC dSph analysis. [25, 26].

528 **7.1.3 Background Estimation**

529 This analysis was done on dwarf spheroidal (dSph) galaxies because of their large dark matter
 530 (DM) content relative to baryonic. We consider the following to estimate the background to this
 531 study.

- 532 • The dSphs are small in HAWC’s field of view, so the analysis is not sensitive to large or small
 533 scale anisotropies.
- 534 • The dSphs used in this analysis are off the galactic plane.
- 535 • The dSphs are baryonically faint relative to their expected dark matter content and are not
 536 expected to contain gamma-ray sources.

537 Therefor we make no additional assumptions of the background coming from our sources and
 538 use HAWC’s standard direct integration method for background estimation. It is possible for gamma

539 rays from DM annihilation to scatter in transit to HAWC via Inverse Compton Scattering (ICS).
540 This was investigated and its impact on the flux is basically zero. Supporting information on this
541 is in **TODO: refer to appdx**

542 **7.1.4 Software Tools and Development**

543 This analysis was performed using HAL and 3ML, in Python version 2.[25, 27] Dan developed
544 a source model to implement the *Poor Particle Physicists' Cookbook* (PPPC) [28] into HAWC
545 software. This model and corresponding Monte Carlo simulation was consolidated into a dictionary
546 for other collaborators. A NumPy version of this dictionary was made for both Py2 and Py3. The
547 code base for creating this dictionary is also in Dan's sandbox:

- 548 • Py2: <https://gitlab.com/hawc-observatory/sandboxes/salaza82/glory-duc>
549 k-hawc/-/tree/master/GD_spectrumDictionary Generator (Deprecated)
- 550 • Py3: <https://gitlab.com/hawc-observatory/sandboxes/salaza82/pppc2dictPPPC2Dict>

552 The analysis was performed using the f_{hit} framework performed in the Crab paper[25]. The
553 PPPC model selected for this analysis included electroweak corrections. Dictionaries for the
554 non-electroweak model were generated but not used for this analysis. The Python2 NumPy dictio-
555 nary file for gamma-ray final states is `dmCirSpecDict.npy`. The corresponding Python3 file is
556 `DM_CirrelliSpectrum_dict_gammas.npy`. These files can also be used for decay channels and
557 the PPPC describes how. [28]. Python's pickle is not backwards compatible, so scripts run in Py3
558 are not able to use dictionaries generated using Py2 and vice-versa.

559 All other software used for data analysis, DM profile generation, and job submission to SLURM
560 are also kept in my sandbox for <https://gitlab.com/hawc-observatory/sandboxes/sal>
561 aza82/glory-duck-hawc the Glory Duck project. They're broad descriptions are as follows:

- 562 • `GD_mass_profiles`: scripts that generate .fits maps for HAWC HAL according to [29].
563 Also contains simple plots of these maps.

- 564 • `GD_spectrum`: scripts that generate NumPy dictionaries of PPPC gamma spectra [28].
- 565 • `analysis_scripts`: HAL scripts for performing likelihood computation on HAWC data or
566 simulation with GD spectra and mass profiles.
- 567 • `pointing`: HAL scripts used to compare the impact of point systematic.
- 568 • `poisson_maps`: scripts for generating and managing poisson trials used for this study.

569 **7.2 Analysis**

570 **7.2.1 Monte Carlo Simulation**

571 The expected differential photon flux from a DM-DM annihilation to standard model particles
572 over solid angle is described by the familiar equation.

$$\frac{d\Phi_\gamma}{dE_\gamma} = \frac{\langle\sigma v\rangle}{8\pi m_\chi^2} \frac{dN_\gamma}{dE_\gamma} \times \int_{\text{source}} d\Omega \int_{l.o.s} \rho_\chi^2 dl(r, \theta') \quad (7.1)$$

573 here $\langle\sigma v\rangle$ is the velocity weighted annihilation cross-section. $\frac{dN}{dE}$ is the expected differential number
574 of photons produced at each energy per annihilation. M_χ is the rest mass of the supposed DM
575 particle. J is the astrophysical J-factor and is defined as

576 ρ_χ is the DM density. For this value, we import the PPPC with electroweak corrections [28].
577 The spectrum is implemented as a model script in astromodels for 3ML. The J-factor profiles for
578 each source is imported from Geringer-Sameth (\mathcal{GS}) [30]. Another DM distribution model from
579 Bonnivard (\mathcal{B}) [31] was used for the complete study. However, to save computational time, limits
580 from \mathcal{GS} were scaled to \mathcal{B} instead of each experiment performing a full study a second time. We
581 create NSIDE 16384 maps of the J-factors for each dSph. These maps are integrated over every
582 spatial bin and passed to the fitting software. Plots of these maps are provided for each source in
583 the sandbox directory: `GD_mass_profiles`.

584 **7.2.2 Source Selection and Annihilation Channels**

585 We use many of the dSph presented in our previous dSph DM search [26]. HAWC's sources
586 for Glory Duck include Boötes I, Coma Berenices, Canes Venatici I + II, Draco, Hercules, Leo I,

587 II, + IV, Segue 1, Sextans, and Ursa Major I + II. A full description of all sources used in Glory
 588 Duck is found in Table 7.1. Triangulum II was excluded from the Glory Duck analysis because
 589 of large uncertainties in its J-factor. Ursa Minor was excluded from HAWC’s contribution to the
 590 combination because the source extension model extended Ursa Minor beyond HAWC’s field of
 591 view. Ursa Minor was not expected to contribute significantly to the combined limit, so work was
 592 not invested in a solution to include Ursa Minor.

593 The DM annihilation channels probed for the Glory Duck combination include
 594 $b\bar{b}$, $e\bar{e}$, $\mu\bar{\mu}$, $\tau\bar{\tau}$, $t\bar{t}$, W^+W^- , and ZZ . A summary of all sources, with a description of each ex-
 595 periments’ sensitivity to the source, is provided in Table 7.2.

596 7.2.3 Likelihood Methods

597 We perform a standard HAWC binned maximum likelihood analysis using f_{hit} bins 1-9. This
 598 analysis was performed using HAL and 3ML, in Python2 [25, 27]. With these tools we compute
 599 the max from the likelihood profiles and perform a ratio test to calculate the significance of each
 600 source. This analysis is identical to the previous dSph analysis [26] except the sources are treated
 601 as extended. For the vast majority of our sources, this extension is no greater than 2 degrees. We
 602 calculate the likelihood of each source and model, assuming events are Poisson distributed, with

$$\mathcal{L} = \prod_i \frac{(B_i + S_i)^{N_i} e^{-(B_i + S_i)}}{N_i!} \quad (7.2)$$

603 S_i is the sum of expected number of signal counts. B_i is the number of background counts
 604 observed. N_i is the total number of counts. The i th bin is iterated over spatial and f_{hit} . Then we
 605 combine the profiles across all five experiments. The profile likelihood ratio λ as a function of
 606 annihilation cross-section $\langle\sigma v\rangle$ is computed by:

$$\lambda(\langle\sigma v\rangle | \mathcal{D}_{\text{dSphs}}) = \frac{\mathcal{L}(\langle\sigma v\rangle; \hat{\nu} | \mathcal{D}_{\text{dSphs}})}{\mathcal{L}(\widehat{\langle\sigma v\rangle}; \hat{\nu} | \mathcal{D}_{\text{dSphs}})} \quad (7.3)$$

607 for a considered annihilation channel and DM mass.

608 **TODO: Section pasted from paper. Rephrase cause plagiarism is a thing.** As mentioned pre-
 609 viously, each experiment computes the \mathcal{L}_{lk} from Equation (7.3) differently. The remainder of

Table 7.1 Summary of the relevant properties of the dSphs used in the present work. Column 1 lists the dSphs. Columns 2 and 3 present their heliocentric distance and galactic coordinates, respectively. Columns 4 and 5 report the J -factors of each source given from the \mathcal{GS} and \mathcal{B} independent studies and their estimated $\pm 1\sigma$ uncertainties. The values $\log_{10} J$ (\mathcal{GS} set) [30] correspond to the mean J -factor values for a source extension truncated at the outermost observed star. The values $\log_{10} J$ (\mathcal{B} set) [31] are provided for a source extension at the tidal radius of each dSph. **Bolded sources are within HAWC's field of view and provided to the Glory Duck analysis.**

| Name | Distance (kpc) | l, b ($^{\circ}$) | $\log_{10} J$ (\mathcal{GS} set) $\log_{10}(\text{GeV}^2\text{cm}^{-5}\text{sr})$ | $\log_{10} J$ (\mathcal{B} set) $\log_{10}(\text{GeV}^2\text{cm}^{-5}\text{sr})$ |
|--------------------------|-------------------|--------------------------|---|--|
| Boötes I | 66 | 358.08, 69.62 | $18.24^{+0.40}_{-0.37}$ | $18.85^{+1.10}_{-0.61}$ |
| Canes Venatici I | 218 | 74.31, 79.82 | $17.44^{+0.37}_{-0.28}$ | $17.63^{+0.50}_{-0.20}$ |
| Canes Venatici II | 160 | 113.58, 82.70 | $17.65^{+0.45}_{-0.43}$ | $18.67^{+1.54}_{-0.97}$ |
| Carina | 105 | 260.11, -22.22 | $17.92^{+0.19}_{-0.11}$ | $18.02^{+0.36}_{-0.15}$ |
| Coma Berenices | 44 | 241.89, 83.61 | $19.02^{+0.37}_{-0.41}$ | $20.13^{+1.56}_{-1.08}$ |
| Draco | 76 | 86.37, 34.72 | $19.05^{+0.22}_{-0.21}$ | $19.42^{+0.92}_{-0.47}$ |
| Fornax | 147 | 237.10, -65.65 | $17.84^{+0.11}_{-0.06}$ | $17.85^{+0.11}_{-0.08}$ |
| Hercules | 132 | 28.73, 36.87 | $16.86^{+0.74}_{-0.68}$ | $17.70^{+1.08}_{-0.73}$ |
| Leo I | 254 | 225.99, 49.11 | $17.84^{+0.20}_{-0.16}$ | $17.93^{+0.65}_{-0.25}$ |
| Leo II | 233 | 220.17, 67.23 | $17.97^{+0.20}_{-0.18}$ | $18.11^{+0.71}_{-0.25}$ |
| Leo IV | 154 | 265.44, 56.51 | $16.32^{+1.06}_{-1.70}$ | $16.36^{+1.44}_{-1.65}$ |
| Leo V | 178 | 261.86, 58.54 | $16.37^{+0.94}_{-0.87}$ | $16.30^{+1.33}_{-1.16}$ |
| Leo T | 417 | 214.85, 43.66 | $17.11^{+0.44}_{-0.39}$ | $17.67^{+1.01}_{-0.56}$ |
| Sculptor | 86 | 287.53, -83.16 | $18.57^{+0.07}_{-0.05}$ | $18.63^{+0.14}_{-0.08}$ |
| Segue I | 23 | 220.48, 50.43 | $19.36^{+0.32}_{-0.35}$ | $17.52^{+2.54}_{-2.65}$ |
| Segue II | 35 | 149.43, -38.14 | $16.21^{+1.06}_{-0.98}$ | $19.50^{+1.82}_{-1.48}$ |
| Sextans | 86 | 243.50, 42.27 | $17.92^{+0.35}_{-0.29}$ | $18.04^{+0.50}_{-0.28}$ |
| Ursa Major I | 97 | 159.43, 54.41 | $17.87^{+0.56}_{-0.33}$ | $18.84^{+0.97}_{-0.43}$ |
| Ursa Major II | 32 | 152.46, 37.44 | $19.42^{+0.44}_{-0.42}$ | $20.60^{+1.46}_{-0.95}$ |
| Ursa Minor | 76 | 104.97, 44.80 | $18.95^{+0.26}_{-0.18}$ | $19.08^{+0.21}_{-0.13}$ |

Table 7.2 Summary of dSph observations by each experiment used in this work. A ‘-’ indicates the experiment did not observe the dSph for this study. For Fermi-LAT, the exposure at 1 GeV is given. For HAWC, $|\Delta\theta|$ is the absolute difference between the source declination and HAWC latitude. HAWC is more sensitive to sources with smaller $|\Delta\theta|$. For IACTs, we show the zenith angle range, the total exposure, the energy range, the angular radius θ of the signal or ON region, the ratio of exposures between the background-control (OFF) and signal (ON) regions (τ), and the significance of gamma-ray excess in standard deviations, σ .

| Source name | Fermi-LAT | HAWC | H.E.S.S, MAGIC, VERITAS | | | | | | |
|-------------------|---------------------------------|----------------------|-------------------------|------------|--------------|--------------------|--------------|--------|------------------|
| | Exposure (10^{11} s m 2) | $ \Delta\theta $ (°) | IACT | Zenith (°) | Exposure (h) | Energy range (GeV) | θ (°) | τ | S (σ) |
| Boötes I | 2.6 | 4.5 | VERITAS | 15 – 30 | 14.0 | 100–41000 | 0.10 | 8.6 | -1.0 |
| Canes Venatici I | 2.9 | 14.6 | – | – | – | – | – | – | – |
| Canes Venatici II | 2.9 | 15.3 | – | – | – | – | – | – | – |
| Carina | 3.1 | – | H.E.S.S. | 27 – 46 | 23.7 | 310 – 70000 | 0.10 | 18.0 | -0.3 |
| Coma Berenices | 2.7 | 4.9 | H.E.S.S. | 47 – 49 | 11.4 | 550 – 70000 | 0.10 | 14.4 | -0.4 |
| | | | MAGIC | 5 – 37 | 49.5 | 60 – 10000 | 0.17 | 1.0 | – |
| | | | MAGIC | 29 – 45 | 52.1 | 70 – 10000 | 0.22 | 1.0 | – |
| Draco | 3.8 | 38.1 | VERITAS | 25 – 40 | 49.8 | 120 – 70000 | 0.10 | 9.0 | -1.0 |
| Fornax | 2.7 | – | H.E.S.S. | 11 – 25 | 6.8 | 230 – 70000 | 0.10 | 45.5 | -1.5 |
| Hercules | 2.8 | 6.3 | – | – | – | – | – | – | – |
| Leo I | 2.5 | 6.7 | – | – | – | – | – | – | – |
| Leo II | 2.6 | 3.1 | – | – | – | – | – | – | – |
| Leo IV | 2.4 | 19.5 | – | – | – | – | – | – | – |
| Leo V | 2.4 | – | – | – | – | – | – | – | – |
| Leo T | 2.6 | – | – | – | – | – | – | – | – |
| Sculptor | 2.7 | – | H.E.S.S. | 10 – 46 | 11.8 | 200 – 70000 | 0.10 | 19.8 | -2.2 |
| Segue I | 2.5 | 2.9 | MAGIC | 13 – 37 | 158.0 | 60 – 10000 | 0.12 | 1.0 | -0.5 |
| | | | VERITAS | 15 – 35 | 92.0 | 80 – 50000 | 0.10 | 7.6 | 0.7 |
| Segue II | 2.7 | – | – | – | – | – | – | – | – |
| Sextans | 2.4 | 20.6 | – | – | – | – | – | – | – |
| Ursa Major I | 3.4 | 32.9 | – | – | – | – | – | – | – |
| Ursa Major II | 4.0 | 44.1 | MAGIC | 35 – 45 | 94.8 | 120 – 10000 | 0.30 | 1.0 | -2.1 |
| Ursa Minor | 4.1 | – | VERITAS | 35 – 45 | 60.4 | 160 – 93000 | 0.10 | 8.4 | -0.1 |

610 this section highlights the differences in this calculation across the experiments. Four experiments,
 611 namely *Fermi*-LAT, H.E.S.S., HAWC and MAGIC, use a binned likelihood to compute the \mathcal{L}_{lk} . For
 612 these experiments, for each observation \mathcal{D}_{lk} of a given dSph l carried out using a given gamma-ray
 613 detector k , the binned likelihood function is:

$$\mathcal{L}_{lk}(\langle\sigma v\rangle; J_l, \nu_{lk} | \mathcal{D}_{lk}) = \prod_{i=1}^{N_E} \prod_{j=1}^{N_P} \left[\mathcal{P}(s_{lk,ij}(\langle\sigma v\rangle, J_l, \nu_{lk}) + b_{lk,ij}(\nu_{lk}) | N_{lk,ij}) \right] \times \mathcal{L}_{lk,\nu}(\nu_{lk} | \mathcal{D}_{\nu_{lk}}) \quad (7.4)$$

615 where N_E and N_P are the number of considered bins in reconstructed energy and arrival
 616 direction, respectively; \mathcal{P} represents a Poisson PDF for the number of gamma-ray candidate events
 617 $N_{lk,ij}$ observed in the i -th bin in energy and j -th bin in arrival direction, when the expected number
 618 is the sum of the expected mean number of signal events s_{ij} (produced by DM annihilation) and of
 619 background events b_{ij} ; $\mathcal{L}_{lk,\nu}$ is the likelihood term for the extra ν_{lk} nuisance parameters that vary
 620 from one instrument k to another. The expected counts for signal events s_{ij} for a given dSph l and
 621 detector k is given by:

$$s_{ij}(\langle\sigma v\rangle, J) = \int_{E'_{\min,i}}^{E'_{\max,i}} dE' \int_{P'_{\min,j}}^{P'_{\max,j}} d\Omega' \int_0^\infty dE \int_{\Delta\Omega_{tot}} d\Omega \int_0^{T_{\text{obs}}} dt \frac{d^2\Phi(\langle\sigma v\rangle, J)}{dEd\Omega} \text{IRF}(E', P' | E, P, t) \quad (7.5)$$

622 where E' and E are the reconstructed and true energies, P' and P the reconstructed and true
 623 arrival directions; $E'_{\min,i}$, $P'_{\min,j}$, $E'_{\max,i}$, and $P'_{\max,j}$ are their lower and upper limits of the i -th
 624 energy bin and the j -th arrival direction bin; T_{obs} is the (dead-time corrected) total observation
 625 time; t is the time along the observations; $d^2\Phi/dEd\Omega$ is the DM flux in the source region (see
 626 Equation (7.1)); and $\text{IRF}(E', P' | E, P, t)$ is the IRF, which can be factorized as the product of the
 627 effective collection area of the detector $A_{\text{eff}}(E, P, t)$, the PDFs for the energy estimator $f_E(E' | E, t)$,
 628 and arrival direction $f_P(P' | E, P, t)$ estimators. Note that for *Fermi*-LAT, HAWC, MAGIC, and
 629 VERITAS the effect of the finite angular resolution is taken into account through the convolution
 630 of $d\Phi/dEd\Omega$ with f_P in Equation (7.5), whereas in the cases of H.E.S.S. f_P is approximated by a
 631 delta function. This approximation has been made in order to maintain compatibility of the result
 632 with what has been previously published. The difference introduced by this approximation is < 5%

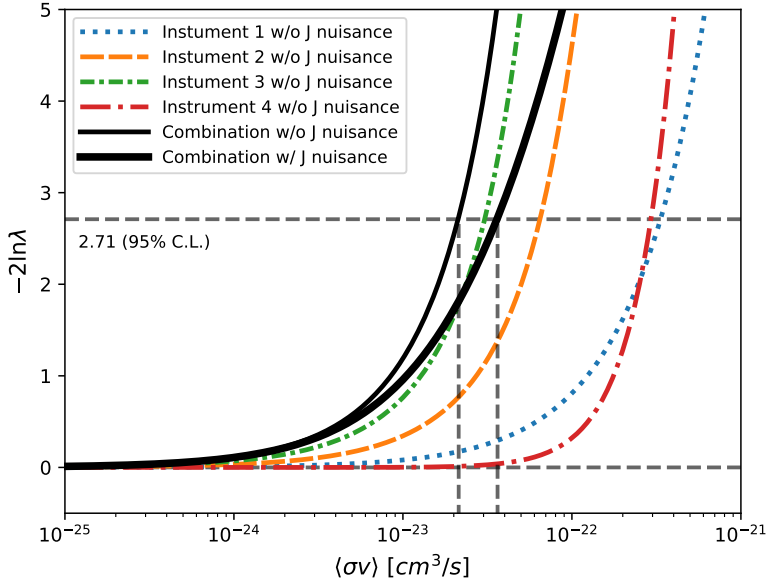


Figure 7.1 Illustration of the combination technique showing a comparison between $-2 \ln \lambda$ provided by four instruments (colored lines) from the observation of the same dSph without any J nuisance and their sum, *i.e.* the resulting combined likelihood (thin black line). According to the test statistics of Equation (7.6), the intersection of the likelihood profiles with the line $-2 \ln \lambda = 2.71$ indicates the 95% C.L. upper limit on $\langle \sigma v \rangle$. The combined likelihood (thin black line) shows a smaller value of upper limit on $\langle \sigma v \rangle$ than those derived by individual instruments. We also show the uncertainties on the J -factor affects the combined likelihood and degrade the upper limit on $\langle \sigma v \rangle$ (thick black line). All likelihood profiles are normalized so that the global minimum $\widehat{\langle \sigma v \rangle}$ is 0. We note that each profile depends on the observational conditions in which a target object was observed. The sensitivity of a given instrument can be degraded and the upper limits less constraining if the observations are performed in non optimal conditions such as a high zenith angle or a short exposure time.

633 for all considered dSphs. **TODO: End of paper section**

634 From Equation (7.3), we can compute the test statistic (TS) with the ratio test:

$$TS = -2 \ln \left(\frac{\mathcal{L}}{\mathcal{L}^{\max}} \right). \quad (7.6)$$

635 \mathcal{L}^{\max} here is equivalent to $\mathcal{L}(N_i, B_i, S_i = 0)$ or no signal counts.

636 7.3 HAWC Results

637 13 of the 20 dSphs considered for the Glory Duck analysis are within HAWC's field of view.

638 These dSph are analyzed for DM content according to the likelihood method described in Sec-

639 tion 7.2.3. The 13 likelihood profiles are then combined to create a combined limit on the dark
640 matter cross-section. This combination is done for 7 of the 8 annihilation channels used in the Glory
641 Duck analysis. Figure 7.2 shows the combined limit for all annihilation channels with HAWC only
642 observations. We also perform 300 studies of Poisson trials on the background. These trials are
643 used to produce HAWC Brazil bands are shared with the other collaborators for combined Brazil
644 Bands. The results on fitting to HAWC’s poisson trials of the DM hypothesis is shown in Figure 7.3
645 for seven of the DM annihilation channels.

646 No DM was found in HAWC observations. The limits are dominated by the dSph Segue1 and
647 Coma Berenices. The remaining 11 dSphs do no contribute significantly to the limit. Even though
648 the remaining dSphs have large J-factors, they are towards the edge of HAWC’s field of view where
649 this analysis is less sensitive.

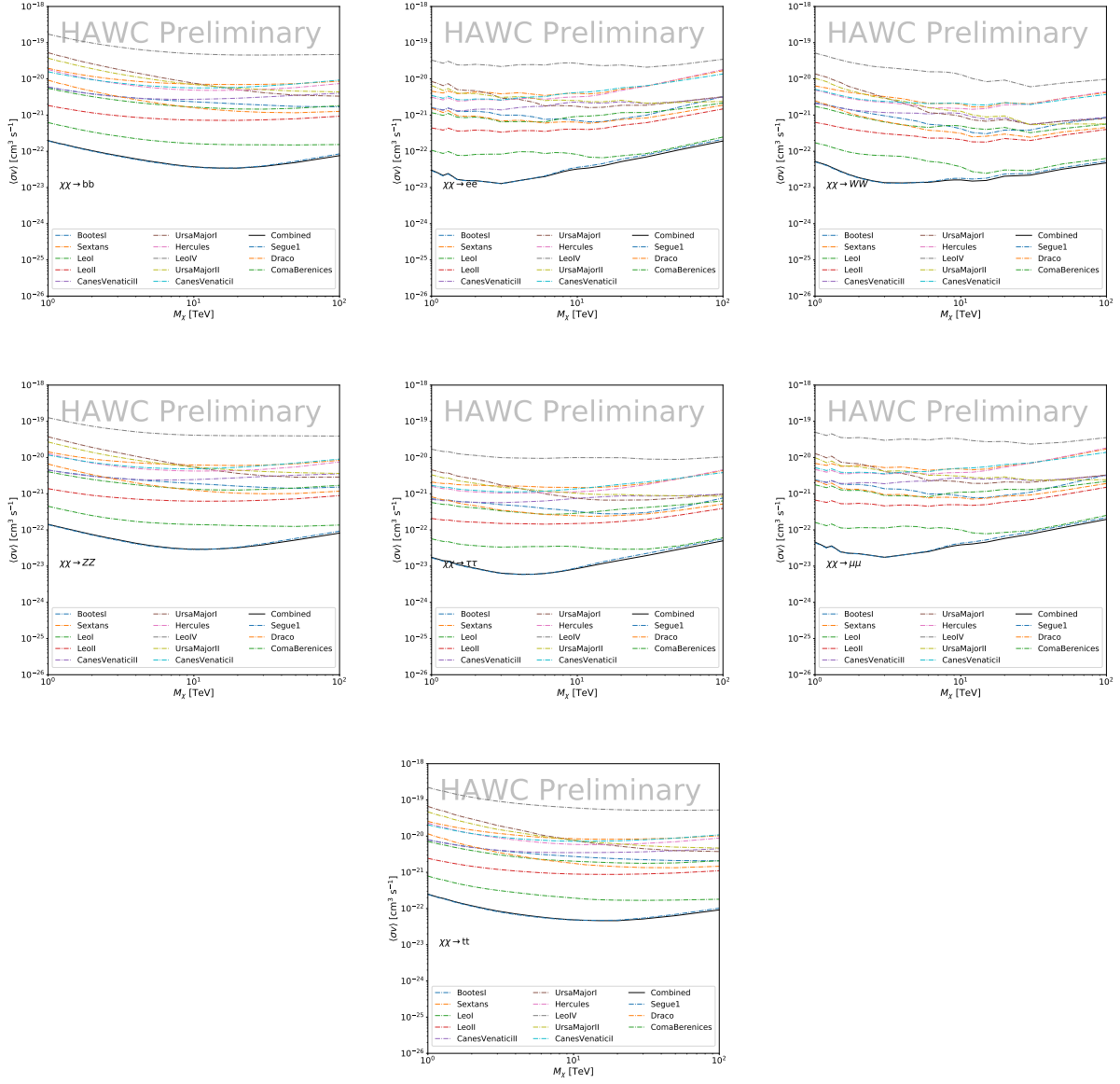


Figure 7.2 HAWC upper limits at 95% confidence level on $\langle\sigma v\rangle$ versus DM mass for seven annihilation channels, using the set of J -factors from Ref. [29]. The solid line represents the observed combined limit. Dashed lines represent limits from individual dSphs.

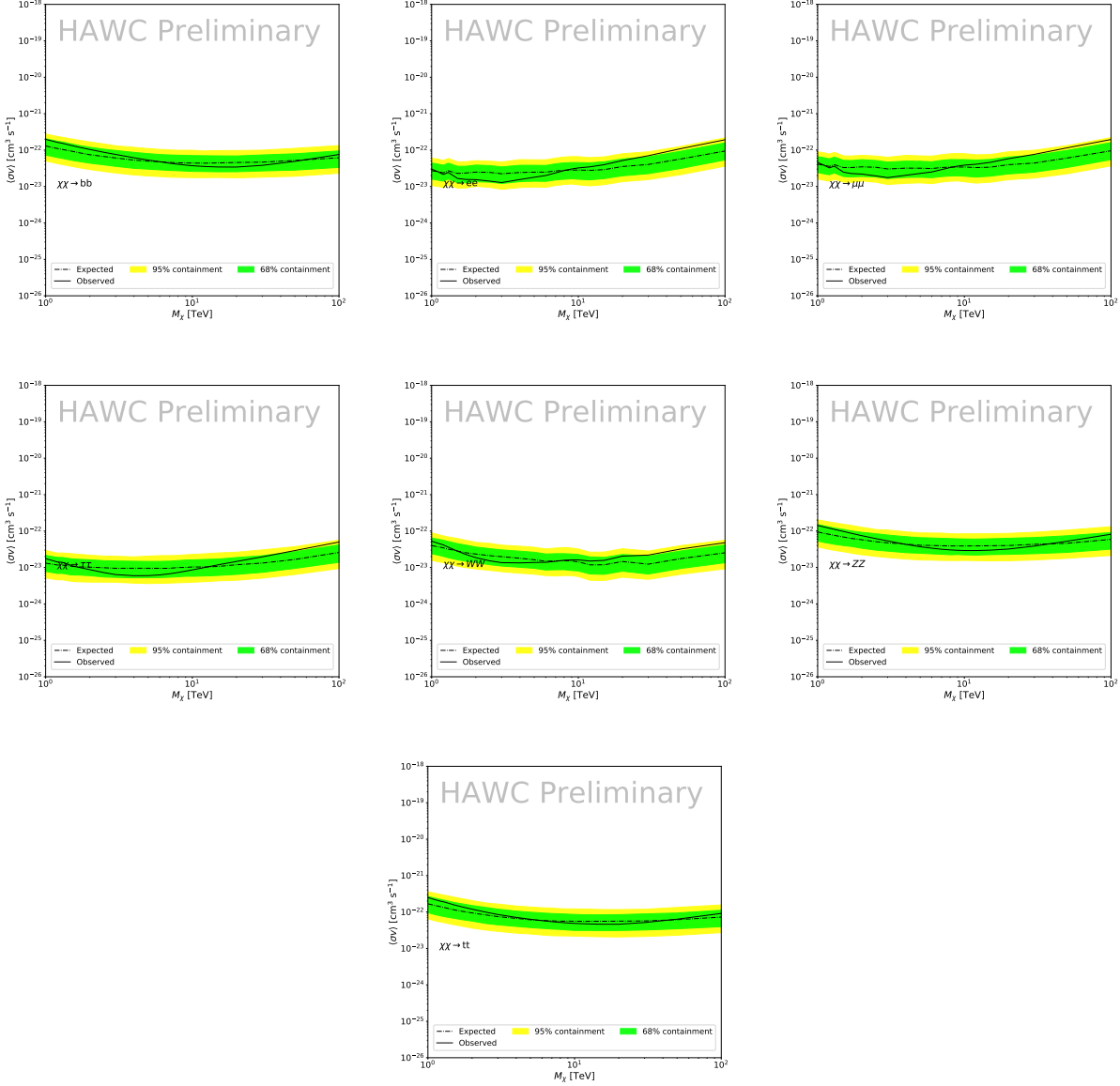


Figure 7.3 HAWC Brazil bands at 95% confidence level on $\langle\sigma v\rangle$ versus DM mass for seven annihilation channels with J -factors from \mathcal{GS} [29]. The solid line represents the combined limit from 13 dSphs. The dashed line is the expected limit. The green band is the 68% containment. The yellow band is the 95% containment.

CHAPTER 8

NU DUCK

650

BIBLIOGRAPHY

- 652 [1] Anne M. Green. “Dark matter in astrophysics/cosmology”. In: *SciPost Phys. Lect.*
 653 *Notes* (2022), p. 37. doi: [10.21468/SciPostPhysLectNotes.37](https://doi.org/10.21468/SciPostPhysLectNotes.37). URL: <https://scipost.org/10.21468/SciPostPhysLectNotes.37>.
- 655 [2] Bing-Lin Young. “A survey of dark matter and related topics in cosmology”. In: *Frontiers*
 656 *of Physics* 12 (Oct. 2016). doi: <https://doi.org/10.1007/s11467-016-0583-4>.
 657 URL: <https://doi.org/10.1007/s11467-016-0583-4>.
- 658 [3] Gianfranco Bertone, Dan Hooper, and Joseph Silk. “Particle dark matter: evidence,
 659 candidates and constraints”. In: *Physics Reports* 405.5 (2005), pp. 279–390. ISSN:
 660 0370-1573. doi: <https://doi.org/10.1016/j.physrep.2004.08.031>. URL:
 661 <https://www.sciencedirect.com/science/article/pii/S0370157304003515>.
- 662 [4] Gianfranco Bertone and Dan Hooper. “History of dark matter”. In: *Rev. Mod. Phys.*
 663 90 (4 Aug. 2018), p. 045002. doi: [10.1103/RevModPhys.90.045002](https://doi.org/10.1103/RevModPhys.90.045002). URL: <https://link.aps.org/doi/10.1103/RevModPhys.90.045002>.
- 665 [5] Fritz Zwicky. “The Redshift of Extragalactic Nebulae”. In: *Helvetica Physica Acta* 6.
 666 (1933), pp. 110–127. doi: [10.5169/seals-110267](https://doi.org/10.5169/seals-110267).
- 667 [6] Vera C. Rubin and Jr. Ford W. Kent. “Rotation of the Andromeda Nebula from a
 668 Spectroscopic Survey of Emission Regions”. In: *ApJ* 159 (Feb. 1970), p. 379. doi:
 669 [10.1086/150317](https://doi.org/10.1086/150317).
- 670 [7] K. G. Begeman, A. H. Broeils, and R. H. Sanders. “Extended rotation curves of spiral galax-
 671 ies: dark haloes and modified dynamics”. In: *Monthly Notices of the Royal Astronomical So-*
 672 *ciety* 249.3 (Apr. 1991), pp. 523–537. ISSN: 0035-8711. doi: [10.1093/mnras/249.3.523](https://doi.org/10.1093/mnras/249.3.523).
 673 eprint: <https://academic.oup.com/mnras/article-pdf/249/3/523/18160929/mnras249-0523.pdf>. URL: <https://doi.org/10.1093/mnras/249.3.523>.
- 675 [8] *Different types of gravitational lenses*. website. Feb. 2004. URL: <https://esahubble.org/images/heic0404b/>.
- 677 [9] Douglas Clowe et al. “A Direct Empirical Proof of the Existence of Dark Matter”. In: *apjl*
 678 648.2 (Sept. 2006), pp. L109–L113. doi: [10.1086/508162](https://doi.org/10.1086/508162). arXiv: [astro-ph/0608407](https://arxiv.org/abs/astro-ph/0608407)
 679 [*astro-ph*].
- 680 [10] Planck Collaboration and N. et. al. Aghanim. “Planck 2018 results I. Overview and the
 681 cosmological legacy of Planck”. In: *A&A* 641 (2020). doi: [10.1051/0004-6361/201833880](https://doi.org/10.1051/0004-6361/201833880). URL: <https://doi.org/10.1051/0004-6361/201833880>.
- 683 [11] Wayne Hu. *Matter Density Animation*. web. 2024. URL: <http://background.uchicago.edu/~whu/animbut/anim2.html>.

- 685 [12] Wenlong Yuan et al. “A First Look at Cepheids in a Type Ia Supernova Host with JWST”. in:
686 *The Astrophysical Journal Letters* 940.1 (Nov. 2022). doi: [10.3847/2041-8213/ac9b27](https://doi.org/10.3847/2041-8213/ac9b27).
687 URL: <https://dx.doi.org/10.3847/2041-8213/ac9b27>.
- 688 [13] Wendy L. Freedman. “Measurements of the Hubble Constant: Tensions in Perspective”. In:
689 *The Astrophysical Journal* 919.1 (Sept. 2021), p. 16. doi: [10.3847/1538-4357/ac0e95](https://doi.org/10.3847/1538-4357/ac0e95).
690 URL: <https://dx.doi.org/10.3847/1538-4357/ac0e95>.
- 691 [14] Jodi Cooley. “Dark Matter direct detection of classical WIMPs”. In: *SciPost Phys. Lect.
692 Notes* (2022), p. 55. doi: [10.21468/SciPostPhysLectNotes.55](https://doi.org/10.21468/SciPostPhysLectNotes.55). URL: <https://scipost.org/10.21468/SciPostPhysLectNotes.55>.
- 693 [15] “Search for new phenomena in events with an energetic jet and missing transverse momentum
694 in pp collisions at $\sqrt{s} = 13$ TeV with the ATLAS detector”. In: *Phys. Rev. D* 103
695 (11 July 2021), p. 112006. doi: [10.1103/PhysRevD.103.112006](https://doi.org/10.1103/PhysRevD.103.112006). URL: <https://link.aps.org/doi/10.1103/PhysRevD.103.112006>.
- 696 [16] *Jetting into the dark side: a precision search for dark matter*. website. July 2020. URL:
697 <https://atlas.cern/updates/briefing/precision-search-dark-matter>.
- 700 [17] Celine Armand et. al. “Combined dark matter searches towards dwarf spheroidal galaxies
701 with Fermi-LAT, HAWC, H.E.S.S., MAGIC, and VERITAS”. in: *Proceedings of Science*.
702 Vol. 395. Mar. 2022. doi: <https://doi.org/10.22323/1.395.0528>.
- 703 [18] Tracy R. Slatyer. “Les Houches Lectures on Indirect Detection of Dark Matter”. In: *SciPost
704 Phys. Lect. Notes* (2022), p. 53. doi: [10.21468/SciPostPhysLectNotes.53](https://doi.org/10.21468/SciPostPhysLectNotes.53). URL:
705 <https://scipost.org/10.21468/SciPostPhysLectNotes.53>.
- 706 [19] Christian W Bauer, Nicholas L. Rodd, and Bryan R. Webber. “Dark matter spectra from
707 the electroweak to the Planck scale”. In: *Journal of High Energy Physics* 2021.1029-8479
708 (June 2021). doi: [https://doi.org/10.1007/JHEP06\(2021\)121](https://doi.org/10.1007/JHEP06(2021)121).
- 709 [20] Riccardo Catena and Piero Ullio. “A novel determination of the local dark matter density”.
710 In: *Journal of Cosmology and Astroparticle Physics* 2010.08 (Aug. 2010), p. 004. doi:
711 [10.1088/1475-7516/2010/08/004](https://doi.org/10.1088/1475-7516/2010/08/004). URL: <https://dx.doi.org/10.1088/1475-7516/2010/08/004>.
- 713 [21] B. P. Abbott et al. “Observation of Gravitational Waves from a Binary Black Hole Merger”.
714 In: *Phys. Rev. Lett.* 116 (6 Feb. 2016), p. 061102. doi: [10.1103/PhysRevLett.116.061102](https://doi.org/10.1103/PhysRevLett.116.061102). URL: <https://link.aps.org/doi/10.1103/PhysRevLett.116.061102>.
- 715 [22] R. Abbasi et. al. “Observation of high-energy neutrinos from the Galactic plane”. In: *Science*
716 380.6652 (June 2023), pp. 1338–1343.
- 718 [23] NASA Goddard Space Flight Center. *Fermi’s 12-year view of the gamma-ray sky*. website.

- 719 2022. URL: <https://svs.gsfc.nasa.gov/14090>.
- 720 [24] Marco Cirelli et al. “PPPC 4 DM ID: a poor particle physicist cookbook for dark matter
721 indirect detection”. In: *Journal of Cosmology and Astroparticle Physics* 2011.03 (Mar.
722 2011), p. 051. doi: [10.1088/1475-7516/2011/03/051](https://dx.doi.org/10.1088/1475-7516/2011/03/051). URL: <https://dx.doi.org/10.1088/1475-7516/2011/03/051>.
- 724 [25] A. U. Abeysekara et al. “Observation of the Crab Nebula with the HAWC Gamma-Ray
725 Observatory”. In: *The Astrophysical Journal* 843.1 (June 2017), p. 39. doi: [10.3847/1538-4357/aa7555](https://doi.org/10.3847/1538-4357/aa7555). URL: <https://doi.org/10.3847/1538-4357/aa7555>.
- 727 [26] A. Albert et al. “Dark Matter Limits from Dwarf Spheroidal Galaxies with the HAWC
728 Gamma-Ray Observatory”. In: *The Astrophysical Journal* 853.2 (Feb. 2018), p. 154. ISSN:
729 1538-4357. doi: [10.3847/1538-4357/aaa6d8](https://dx.doi.org/10.3847/1538-4357/aaa6d8). URL: [http://dx.doi.org/10.3847/1538-4357/aaa6d8](https://dx.doi.org/10.3847/1538-4357/aaa6d8).
- 731 [27] Giacomo Vianello et al. *The Multi-Mission Maximum Likelihood framework (3ML)*. 2015.
732 arXiv: [1507.08343](https://arxiv.org/abs/1507.08343) [astro-ph.HE].
- 733 [28] Marco Cirelli et al. “PPPC 4 DM ID: a poor particle physicist cookbook for dark matter
734 indirect detection”. In: *Journal of Cosmology and Astroparticle Physics* 2011.03 (Mar.
735 2011). ISSN: 1475-7516. doi: [10.1088/1475-7516/2011/03/051](https://dx.doi.org/10.1088/1475-7516/2011/03/051). URL: [http://dx.doi.org/10.1088/1475-7516/2011/03/051](https://dx.doi.org/10.1088/1475-7516/2011/03/051).
- 737 [29] Alex Geringer-Sameth, Savvas M. Koushiappas, and Matthew Walker. “Dwarf galaxy
738 annihilation and decay emission profiles for dark matter experiments”. In: *Astrophys.
739 J.* 801.2 (2015), p. 74. doi: [10.1088/0004-637X/801/2/74](https://dx.doi.org/10.1088/0004-637X/801/2/74). arXiv: [1408.0002](https://arxiv.org/abs/1408.0002)
740 [astro-ph.CO].
- 741 [30] Alex Geringer-Sameth, Savvas M. Koushiappas, and Matthew Walker. “DWARF GALAXY
742 ANNIHILATION AND DECAY EMISSION PROFILES FOR DARK MATTER EXPERI-
743 MENTS”. in: *The Astrophysical Journal* 801.2 (Mar. 2015), p. 74. ISSN: 1538-4357. doi:
744 [10.1088/0004-637X/801/2/74](https://dx.doi.org/10.1088/0004-637X/801/2/74). URL: [http://dx.doi.org/10.1088/0004-637X/801/2/74](https://dx.doi.org/10.1088/0004-637X/801/2/74).
- 746 [31] V. Bonnivard et al. “Spherical Jeans analysis for dark matter indirect detection in dwarf
747 spheroidal galaxies - Impact of physical parameters and triaxiality”. In: *Mon. Not. Roy.
748 Astron. Soc.* 446 (2015), pp. 3002–3021. doi: [10.1093/mnras/stu2296](https://doi.org/10.1093/mnras/stu2296). arXiv:
749 [1407.7822](https://arxiv.org/abs/1407.7822) [astro-ph.HE].